Water vapor on Mars: a refined climatology and constraints on the near-surface concentration enabled by synergistic retrievals

Elise W. Knutsen[1], Franck Montmessin[1], Loic Verdier[1], Gaétan Lacombe[1], Franck Lefèvre[1], Stéphane Ferron[2], Marco Giuranna[3], Paulina Wolkenberg[3], Anna Fedorova[4], Alexander Trokhimovskiy[4], Oleg Korablev[4]

[1]LATMOS/IPSL, UVSQ Université Paris-Saclay, Sorbonne Université, CNRS, Guyancourt, France

[2]ACRI-ST, boulevard des Garennes, Guyancourt, France

[3]IAPS-INAF, Rome, Italy

[4]Space Research Institute (IKI), Moscow, Russia

Corresponding author: Elise Wright Knutsen (elise-wright.knutsen@latmos.ipsl.fr)

Key Points:

- Using a spectral synergy retrieval method on nadir observations from SPICAM and PFS to obtain a highly accurate water vapor climatology.
- The synergy method is sensitive to the vertical distribution of H_2O, and can distinguish near-surface water from the rest of the column.
- Discrepancies in meridional and seasonal behavior of vertical confinement are revealed between the synergy and the Mars Climate Database.

Abstract

With the utilization of a novel synergistic approach, we constrain the vertical distribution of water vapor on Mars with measurements from nadir-pointing instruments. Water vapor column abundances were retrieved simultaneously with PFS (sensing the thermal infrared range) and SPICAM (sensing the near-infrared range) on Mars Express, yielding distinct yet complementary sensitivity to different parts of the atmospheric column. We show that by exploiting a spectral synergy retrieval approach, we obtain more accurate water vapor column abundances compared to when only one instrument is used, providing a new and highly robust reference climatology from Mars Express. We present a composite global dataset covering all seasons and latitudes, assembled from co-located observations sampled from seven Martian years. The synergy also offers a way to study the vertical partitioning of water, which has remained out of the scope of nadir observations made by single instruments covering a single spectral interval. Special attention is given to the north polar region, with extra focus on the sublimation of the seasonal polar cap during the late spring and summer seasons. Column abundances from the Mars Climate Database were found to be significantly higher than synergistically retrieved values, especially in the summer Northern Hemisphere. Deviations between synergy and model in both magnitude and meridional variation of the vertical confinement were also discovered, suggesting that certain aspects of the transport and dynamics of water vapor are not fully captured by current models.

Plain Language Summary

Water vapor plays an important role in the weather and climate on Mars, even though little of it remains today. The behavior of water vapor has been studied for decades, yet how water vapor varies with altitude, especially close to the surface, remains an open question. In this study, we use measurements from two instruments on the Mars Express satellite to learn about the near-surface water vapor. By combining measurements from the SPICAM and PFS spectrometers, a composite full-year climatology is assembled. We measure the total amount of water vapor with great accuracy, and also obtain information about the vertical distribution. The north polar cap is studied in detail during early summer, when part of the polar ice cap sublimates into water vapor and is transported south. The results are compared to model data from the Mars Climate Database, and significant differences between the observations and the model are identified. The total water content is found to be smaller than model estimates, while observations indicate that more water than expected is confined near the surface. This suggests that some aspects of the atmospheric transport processes are not currently fully understood.

1 Introduction

Water vapor on Mars was first detected in 1963 with the use of a ground-based telescope which observed eleven near-infrared absorption lines (Spinrad et al., 1963). Since then, numerous observatories, ground-based, Earth-orbiting, Mars-orbiting, landers and rovers, have observed the highly volatile trace gas. Even as a minor atmospheric constituent, water vapor plays a major role in shaping the climate on Mars (along with the CO_2 and dust cycles). Water controls the stability of the atmosphere, as H_2O photolysis supplies hydroxyl radicals, the main oxidant of the

Martian photochemical cycle (e.g. McElroy and Donahue (1972)), and impacts the radiative equilibrium through cloud formation (Madeleine et al., 2012).

The Mars Atmospheric Water Detector (MAWD) instruments on the Viking orbiters provided evidence that the Northern polar cap is the primary source of atmospheric water, and also indicated a strong north–south asymmetry in the atmospheric water abundance (Farmer et al., 1976; Jakosky & Farmer, 1982). The most complete climatology, upon which modern Martian water climatology is based, was obtained by the Mars Global Surveyor mission and its Thermal Emission Spectrometer (Smith, 2002, 2004). A revised retrieval scheme on TES observations provide an annual reference water vapor cycle with column abundance maximum at high latitudes during midsummer in both hemispheres, reaching a peak of ~60 pr-μm on average in the north, and ~25 pr-μm in the south (Pankine et al., 2010). Low water abundances are observed during fall and winter at middle and high latitudes of both hemispheres. General circulation models along with TES observations indicate that water from the southern summer maximum is transported to the Northern Hemisphere (NH) more efficiently than the reverse process (Montmessin et al., 2004; Steele et al., 2014).

One of the main objectives of the Mars Express (MEX) orbiter is to study the water cycle on Mars. Three spectrometers onboard MEX can measure the water vapor abundance in different spectral bands: The Planetary Fourier Spectrometer (PFS), The Observatoire pour la Minéralogie, l'Eau, les Glaces, et l'Activité (OMEGA) and SPectroscopy for the Investigation of the Characteristics of the Atmosphere of Mars (SPICAM). For the purpose of this study, PFS was selected for its coverage of water vapor diagnostic features in the thermal infrared (TIR) domain, while SPICAM was chosen over OMEGA to cover the near infrared (NIR) due to its higher spectral resolution, and the presence of CO_2 bands near the 2.6 μm water feature for OMEGA.

1.1 Water vapor vertical distribution

Until recently, knowledge of the near-surface H_2O profile on Mars mostly relied on general circulation models. The vertical distribution of water vapor has been inferred from nadir measurements (Fouchet et al., 2007; Pankine & Tamppari, 2015) and measured directly by solar occultation viewing geometry with SPICAM on Mars-Express since 2004, and with the ExoMars Trace gas Orbiter (TGO) and its infrared spectrometers NOMAD and ACS since 2018. SPICAM occultation campaigns were not a primary focus of the spacecraft and are therefore not performed very often, whereas TGO, with its orbit adapted for occultation measurements with good vertical and temporal resolution, allows the study of dynamical behavior of water distribution including escape processes in great detail. With this technique, new knowledge has been obtained on the vertical distribution of water in the upper atmosphere as a result of supersaturation above the hygropause, and the occurrence of high altitude water during dust storms (e.g. (Aoki et al., 2019; Fedorova et al., 2020)). SPICAM solar occultations were also used to produce a climatology of vertical distribution covering the Martian years (MY) 27 to 34, that encompassed two global dust events (Fedorova et al., 2021). With solar occultation measurements one can obtain very fine vertical resolution, nevertheless, measurements below 10 km are relatively sparse as aerosol loading in the lower atmosphere leads to high opacities which reduces the transmittance significantly. The lower limit for observation is typically 5-10 km for dust-free conditions, and as high as 20-30 km during the dusty perihelion season (e.g., Aoki et al., (2019)). Only under very clear conditions will solar occultation observations be able to probe

below 10 km, however such conditions mostly occur at high latitudes. As a result, information about the low-atmosphere water vapor profile remains exceptional.

Below 10 km, surface-atmosphere interactions such as convection, frost sublimation and deposition are expected to be the main forcers on the vertical distribution, along with adsorption and desorption. Above 10 km, water ice clouds are thought to be dominant (Montmessin et al., 2004; Richardson, 2002). Below the saturation level, controversy exists regarding whether water vapor is well mixed with CO_2, or distributed in a more complex manner. Davies (1979) used Viking Orbiter 1 data to directly probe the location of water vapor with altitude for the first time. He found that H_2O vertical distribution was indistinguishable from the dust vertical distribution and was well mixed up to about 10 km, which has been commonly assumed since. Recent analysis of data from the Surface Stereo Imager on the Phoenix lander by Tamppari and Lemmon (2020) show that water is highly confined to a near-surface layer of 2.5 km, and that a well mixed column is not supported by the data. Controversies remain, and it is also argued that water is either confined to, or reduced in the lower atmosphere, depending on season and location. This has relevance to the amount of water vapor exchange occurring between the atmosphere and the regolith.

Adsorption of CO_2 by the Martian regolith was first suggested by Davis et al. (1969), and the theory was later expanded upon to include water vapor by Fanale and Cannon (1971), whose adsorption isotherm expression has been widely used since (although found to require modification by Savijärvi and Harri (2021)). Using data from Viking 1 and 2, Jakosky et al. (1997) showed a nocturnal depletion of atmospheric water vapor, suggesting a diurnal exchange cycle between the porous regolith and the atmosphere. Similar results were obtained with the thermal and electrical conductivity probe on the Phoenix lander by Zent et al. (2010) and Fischer et al. (2019). It was found that the layer that experiences a diurnal exchange of water with the surface was 0.5–1 km deep (Tamppari et al., 2010). This phenomenon was again confirmed by Harri et al. (2014) and Martínez et al. (2017), who used the REMS-H device on Curiosity rover to derive water vapor volume mixing ratios. Savijärvi and Harri (2021) found that regolith exchange is largely indifferent to surface properties, and that diurnal adsorption/desorption generates approximately 1% variation in the column abundance, which matches Earth analogue measurements very well. Results from Fouchet et al. (2007) indicate that the vertical distribution is controlled by an intermediate state where the water is controlled by atmospheric saturation on one hand, and confined to a surface layer on the other, pointing to significant regolith-atmosphere exchange processes. This result is inferred by investigating the correlation of water columns and pressure, and was not observed directly. Maltagliati et al. (2011) and Trokhimovskiy et al. (2015) also attempted to discern a diurnal exchange process between atmosphere and regolith, but found no evidence of local time variation in H_2O abundances. Thus, the extent of exchange between regolith and atmosphere remains an open question.

1.2 Spectral synergy

When observing an atmosphere in nadir viewing geometry, the outcome is normally a column abundance value of the target species. However, it is possible to obtain information about the vertical distribution of the species by combining multiple spectral domains in the retrieval process. This approach is commonly referred to as a spectral synergy, and was developed for Earth observation by Pan et al. (1995, 1998), who predicted higher sensitivity to near-surface layers of CO if near and thermal infrared spectral bands were combined. This was later confirmed by Edwards et al. (2009), who demonstrated that combining NIR and TIR

measurements in a common retrieval allowed for a significantly higher sensitivity in the troposphere. The method has also been used to increase near-surface sensitivity to other gasses such as CO_2 (Christi & Stephens, 2004), O_3 (Landgraf & Hasekamp, 2007) and CH_4 (Razavi et al., 2009).

TIR measurements are mostly sensitive to the middle atmosphere (at the origin of the photon emission) where the temperature contrast of the atmosphere with respect to the surface is high. NIR measurements on the other hand are sensitive to any molecule present along the column as the technique relies on solar photons traversing the entire atmosphere back and forth. Although Trokhimovskiy et al. (2015) indicate the NIR technique is mostly sensitive to the atmosphere below 30 km, it is only true from a mixing ratio perspective, which favors the denser layers of the atmosphere. In other words, any given change in H_2O mixing ratio will be easier to sense in the bottom of the profile as pressure and number density is assumed to be continuously increasing towards the surface. If seen from a number of molecules perspective, the NIR inversion technique has no preference to a particular position of the column, unless this portion concentrates more water molecules at a specific location. One must note however that dust modulates this assertion. At high dust opacity, part of the incoming flux does not reach the surface and is sent back to space without sampling the entire column. Only in such cases will the NIR technique become altitude dependent.

This difference in sensitivity of NIR and TIR can be viewed as a difference in the shape and peak altitude of the weighting function of water vapor retrieval in a particular wavelength domain, and has been advocated to explain the dispersion of H_2O column abundance values retrieved by the various instruments of MEX (Tschimmel et al., 2008). On the other hand, the difference in sensitivity can also be considered a way to offer simultaneous access to different regions of the atmosphere, leading to the derivation of more than a single parameter representative of the whole column, as is usually the case with instruments that study water vapor using nadir observations. In fact, combining two spectral domains increases the degree of freedom of the signal (DOF). The DOF gives an estimate of the number of independent bits of information in an atmospheric measurement (Rodgers, 2000), and a DOF higher than 1 indicates the presence of some amount of profile shape information.

If attempting to retrieve vertical information with only one instrument, one could argue that as the single instrument is primarily sensitive to a specific altitude region, the obtained vertical confinement is not a “real” partitioning. Instead, the obtained partitioning might be a product of a lack of sensitivity to other, and perhaps wetter, altitude regions, thus producing an artificial vertical partitioning. This problem is avoided with the use of a spectral synergy, as each wavelength interval is susceptible to emission/absorption signatures in separate regions, and therefore obtains information from different altitudes.

This consideration led Montmessin and Ferron (2019) to investigate the potential for a synergistic retrieval of water vapor in the Martian atmosphere using MEX, as the spacecraft constitutes the only asset at Mars observing water in both NIR (SPICAM, OMEGA, PFS) and TIR (PFS) spectral intervals. Despite their differences in field-of-view, sampling and coverage, SPICAM (NIR) and PFS (TIR) were selected for this study as the two have the most extensive records of water vapor retrievals on Mars among the MEX instruments (Fedorova et al., 2006; Fouchet et al., 2007; Giuranna et al., 2019; Trokhimovskiy et al., 2015). As Montmessin and Ferron (2019) concluded on the promising potential for a synergistic retrieval of water vapor on

Mars with MEX, this work is intended to follow-up on this earlier study and present the analysis of a multi-annual dataset covering the period from MY 26 to 34.

The intention of this paper is to be largely descriptive, as this is the first time the spectral synergy has been applied to a larger data set. The numerous implications of the vertical partitioning results, and any differences to other observations or the MCD data base are beyond the scope of this paper, but will be the aim of future work using the synergy. The first part of the manuscript provides an overview of the instruments used in this study (Section 2), and continues in Section 3 with an outline of the synergistic retrieval method, including a description of the selection of measurements within the dataset. The results are presented in Section 4, where in 4.1 a complete synergistic column abundance climatology is presented, followed by a comparison of the column abundance between the synergy, the model and the single spectral domain retrievals are made, before the vertical and spatial distribution is elaborated upon. A discussion of the results and how they compare to previous works follow in Section 5, and Section 6 concludes the findings of this study.

2 Instruments

The Mars Express mission was launched in June 2003, and began nominal science operations in mid-January 2004 (Chicarro et al., 2004), corresponding to the very end of MY 26. From a quasi-polar and highly elliptical orbit with a periapsis of ~300 km and a period of 7.5 hours, MEX has a particularly detailed view of the polar caps at the sublimation onset. With three instruments able to measure the atmospheric water vapor content (OMEGA, PFS, SPICAM), either in the solar reflected or in the thermal component, MEX has delivered a vast amount of valuable data with complete global and seasonal coverage. The PFS and SPICAM instruments cover the thermal and near-infrared domains, respectively, within which water vapor possesses diagnostic signatures.

The measurements used in the following analysis were retrieved from nadir observations, and were selected according to a number of criteria to ensure satisfactory quality of every individual measurement, sufficient geographical and seasonal coverages, and a minimum error of radiative transfer modeling due to surface inhomogeneity (Montmessin & Ferron, 2019). For a detailed description on the selection and averaging processes used for the creation of a dataset compatible with a synergistic extraction of water vapor, the reader is referred to Montmessin and Ferron (2019).

2.1 Mars Express PFS

The Planetary Fourier Spectrometer is an infrared spectrometer with two wavelength channels optimized for atmospheric sensing. The short wavelength channel covers the range 1700-8200 cm^{-1} (~1.22-5.88 µm) with a full width at half maximum (FWHM) of the instantaneous field of view (FOV) of 1.6°, while the long wavelength channel spans the 250-1700 cm^{-1} (5.88-40 µm) with a FWHM FOV of 2.8°, which at the pericenter corresponds to a 440 km^2 surface footprint. Only the long wavelength channel was utilized for this work. Both channels have a spectral resolution of 1.3 cm^{-1}. For further details, see Formisano et al. (2005) and Giuranna et al. (2005).

For the synergistic approach, several windows in the long wavelength channel were selected. The windows from 8-10 µm and 19-25 µm were used to obtain surface temperature and dust model properties, the region at 12-19 µm is dominated by the absorption of the 15 µm CO_2 vibrational transition which was used to retrieve atmospheric temperature profiles, while the 20-

35 μm thermal emission band was used to retrieve the water vapor abundance, henceforth referred to as TIR. Because PFS was used to retrieve several parameters, a high signal-to-noise ratio (SNR) is required, and one individual spectrum obtained with PFS is not satisfactory. Therefore, the retrievals were performed on the average of nine consecutive spectra. The total time passed between the acquisition of the first spectrum to the last of the nine to be averaged is 108 seconds, as it takes 4.5 seconds to acquire a single PFS interferogram and the repetition time is 8.5 seconds (Fouchet et al., 2007). This corresponds to a cumulative surface footprint at the pericenter of 3900 km^2, however note that as the orbit is elliptical, this area will vary depending on spacecraft altitude.

After years of operation, an issue with PFS caused the interferogram peak to not always be centered. The instrument line-shape used here (a sine cardinal function with 1.3 cm^{-1} FWHM) is then not optimal, and could lead to biased water vapor retrievals, with a tendency of being too low. This issue started around orbit 6000 (MY 29), became particularly relevant after orbit 7500 (MY 30), but data obtained in MY 32 and after are less affected. In an effort to largely avoid this problem, we exclude all measurements during MY 30 and MY 31 from further analysis.

2.2 Mars Express SPICAM

The SPICAM UV-IR instrument (Spectroscopy for the Investigation of the Characteristics of the Atmosphere of Mars) is a dual-channel spectrometer designed to study the Martian atmosphere from top to bottom (Bertaux et al., 2006). In this study, only the IR channel was utilized working in the spectral range of 1-1.7 μm with a spectral resolution of 3.5-4.0 cm^{-1}, a complete description of which can be found in Korablev et al. (2006).

In nadir viewing geometry, the IR channel has an instantaneous FOV of 1°, corresponding to a footprint 230 km^2 on the surface when the spacecraft is at the pericenter of its orbit. The incoming flux is separated into two detectors, where detector 1 was used for this work as it provides significantly higher performance in nadir. The wavelength interval 1.34-1.43 μm is defined as the NIR range for the synergy, as it covers the strong water absorption band at 1.38 μm. Averages of ten SPICAM-IR spectra are demonstrated to have a SNR sufficient for reliable retrievals of water vapor column abundances (Fedorova et al., 2006; Trokhimovskiy et al., 2015). For the sake of the synergy, the SPICAM observation closest in time to the center PFS spectrum is selected, and averaged together with the seven previous and the seven following spectra. The 15 spectrum cumulative surface footpring area at pericenter corresponds roughly to 3400 km^2, similar to that of the nine PFS spectrum average. Together, the SPICAM and PFS average spectra constitute a co-located observation.

3 Data set and retrieval

In the earlier demonstration of the synergy method applied to Martian water vapor, a subset of 449 co-located observations from 133 orbits distributed through MY 27 were presented (Montmessin & Ferron, 2019), showcasing that the synergy brings additional robustness to the retrieval of water vapor column abundance, and provides insight into the vertical distribution of water vapor. In this study, we expand on those findings, and conduct a comprehensive analysis of the complete synergistic dataset available from MEX, which at the time of writing contains nearly 200 000 measurements.

The dataset presented here consists of co-located observations taken over 1379 individual orbits distributed across seven Mars years from Ls 334° of MY 26 to Ls 297° of MY 34, with no

measurements from MY 30-31 (Knutsen, 2022). The geographical and seasonal coverage is highly variable from year to year, several being quite sparsely covered. Some sparsity is due to operational constraints, as not all instruments can be concurrently active, while most is due to the requirement of co-located measurements from both SPICAM and PFS.

3.1 Synergistic retrieval routine

The synergistic approach requires a set of co-located PFS and SPICAM observations on which to apply the retrieval method. To obtain a satisfying PFS SNR for the fitting of multiple parameters, nine consecutive spectra are averaged together. The SPICAM observation closest in time to the central PFS spectrum is then selected and averaged with the seven observations prior to it and the seven after it, resulting in a combined FOV similar to that of the nine combined PFS observations. A screening process is conducted on this set of co-located observations, the details of which can be found in Montmessin and Ferron (2019). The simultaneous inversion of H_2O follows the approach outlined in Montmessin and Ferron (2019), and will only be briefly described here.

A priori water vapor and temperature profiles are extracted from the Mars Climate Database (MCD) based on the general circulation model developed at the Laboratoire de Météorologie Dynamique (LMD GCM) (Forget et al., 1999; Millour et al., 2018) with an uncertainty of the water equal to the abundance values. MCD version 5.3 is used. For each year the corresponding scenario is chosen, except for MY 34, which is not yet included (the version used was last updated on 11/01/2019). A composite scenario was therefore built for MY 34 by combining the scenario of MY 33 with the standard MCD dust storm scenario 4 and the warm and dusty scenario 7 (for the intervals Ls=180°-200° and Ls=200°-220° respectively).

Temperature and aerosol parameters are retrieved individually from the PFS average spectra, which are then injected into the synergistic routine. The overall spectral fitting procedure uses the HITRAN 2012 spectroscopic database (Rothman et al., 2013) as a baseline for the computation of absorption coefficients of H_2O and CO_2, and then relies on a Bayesian approach that consists in maximizing the probability that a given retrieval satisfies both the observed averaged spectra and falls within a range of plausible a priori values specified by assumptions on the value and its dispersion. The weight of the a priori assumption in the retrieval is dictated by its a priori uncertainty, which is set equal to the integrated a priori water vapor profile.

Water vapor is inferred from the set of combined NIR and TIR spectra, by a simultaneous inversion from both spectral domains. In practice, the algorithm adjusts the water vapor abundance along the vertical profile at nine altitude points separated by 2.5 km from ground to 10 km, and by 5 km from 10 to 30 km. All points are correlated with a Gaussian kernel, such that the points are less strongly correlated when the distance between them is increasing. The results include a posteriori covariance matrix, from which the DOF can be calculated from the sum of the trace of the matrix. The DOF normally fluctuates around 1 when the retrieval includes a single spectral domain (NIR or TIR), which implies only one independent parameter can be inferred from a water vapor measurement (e.g. the CIA), while with a higher DOF some information of the water vapor vertical distribution can be obtained.

Some example spectra are shown in the top row of Figure 1, where the selected NIR and TIR spectral intervals include strong diagnostic features of water vapor. The co-located observations shown here are from early summer of MY 27 at high latitudes. The corresponding vertical profile obtained from the synergistic retrieval performed on both spectra is shown in the bottom left, and

is compared to the MCD a priori profile. In the bottom center and bottom right plots, the synergy is compared to the single spectral domain retrievals in terms of averaging kernels (bottom center) and the posterior-to-prior error ratio profiles (bottom right). MCD a priori profiles are used for all retrieval techniques (synergy, PFS-only, SPICAM-only), such that the a posteriori-to-a priori (post-to-prior for short) error profiles are ratios at each altitude level of the retrieved posteriori error and the MCD a priori error. The post-to-prior profile indicates the amount of added information at each altitude, and shows that the synergy is more sensitive to the lower atmosphere than both PFS and SPICAM.

We quantify the amount of information added by the synergy at each altitude level by comparing the synergistically retrieved error profiles to the MCD a priori error profiles, shown in the bottom right panel of Figure 1. In this way, we demonstrate that the synergy does not simply reproduce the a priori when calculating vertical profiles, and that for the lower atmosphere, the synergy brings more information than the single spectral domain retrievals. The MCD a priori and the retrieved vertical mixing ratio profiles are close to identical above 15 km, but start to deviate below this, where the synergy provides a significant amount of added information.

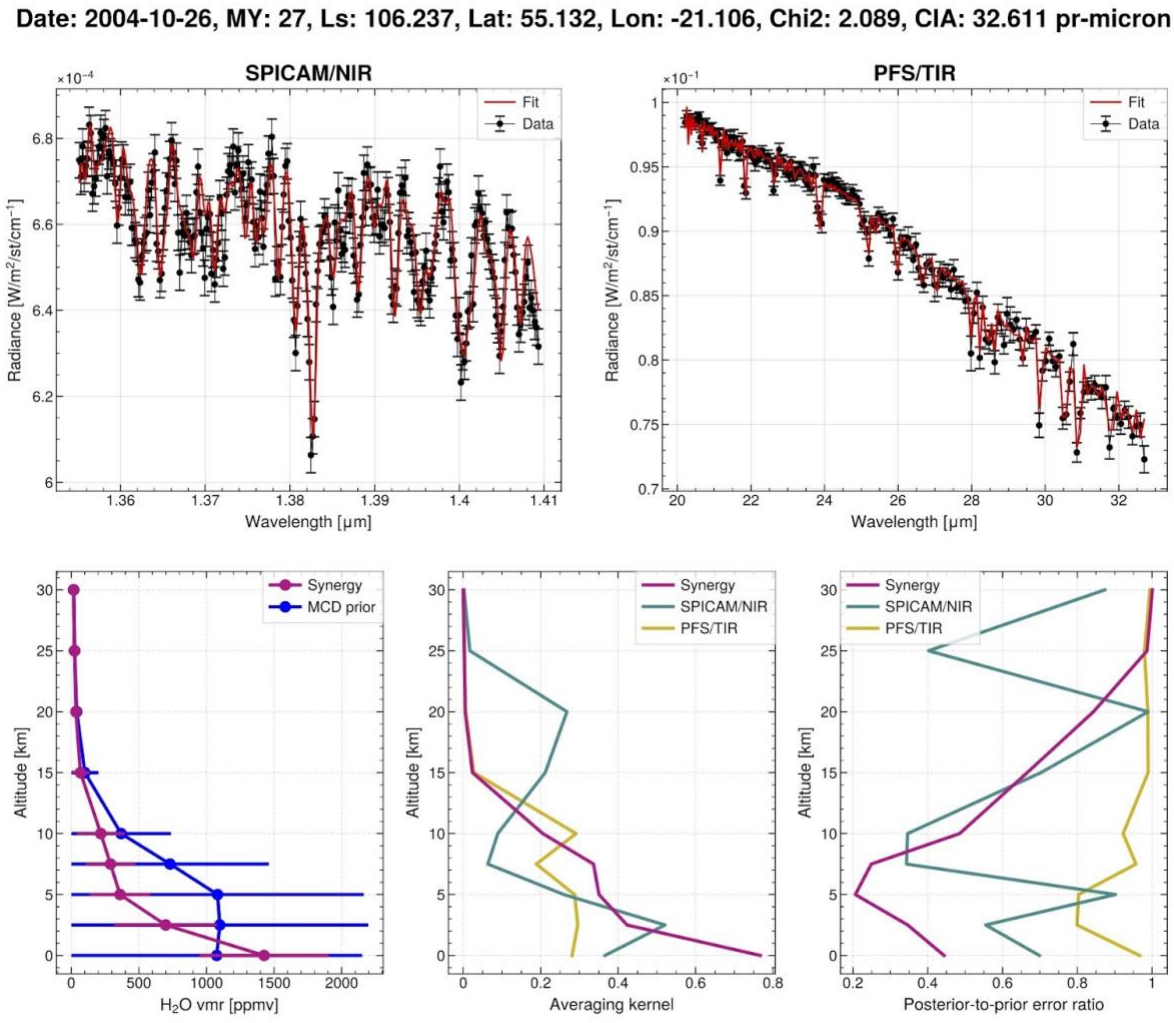

Figure 1: Typical example of averaged spectra from observations in the northern hemisphere high latitudes during early summer, with the corresponding vertical profile of water vapor

mixing ratio and a demonstration of sensitivity along the vertical for the synergy. Top left) SPICAM-IR spectrum. Top right) Averaged PFS spectrum. Data in black and fit in red for both panels. Bottom left) Vertical profile of water vapor as obtained from simultaneous retrieval of both spectral domains, along with the MCD a priori vertical profile. Bottom center) Averaging kernel for retrieval made with the spectral synergy method, SPICAM/NIR, and PFS/TIR. Bottom right) post-to-prior error ratio by altitude for synergistic retrieval and single spectral domain retrievals.

3.2 Data selection scheme

The complete synergy dataset is shown in Figure 2, where the seasonal coverage for all synergy column abundance retrievals are displayed as a function of latitude. Retrievals from MY 27 encompass more than 30% of all co-located observations. The total water columns here are not corrected for topography.

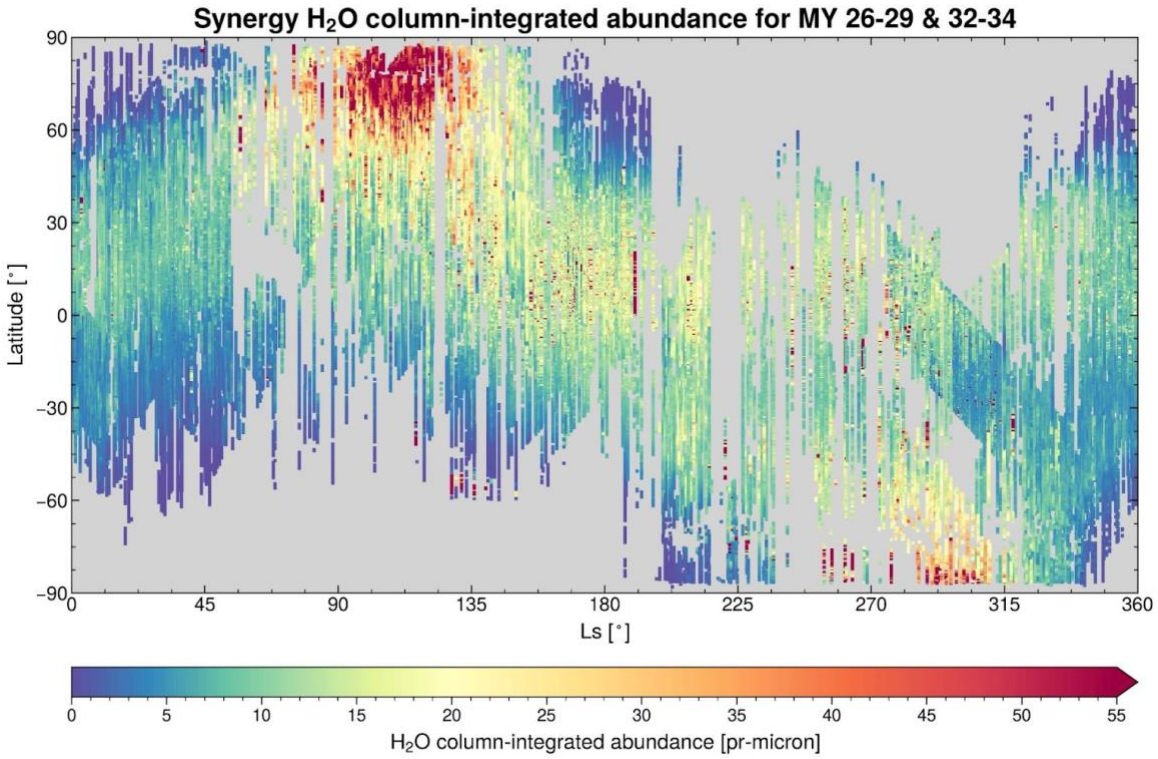

Figure 2: Total column-integrated abundance shown as a function of season and latitude. The figure includes all data points in the synergy dataset. Note that no binning or selection has been done, and data points are partially overlapping with more recent observations on top.

Several selection criteria were applied to the PFS and SPICAM measurements when assembling the synergy dataset, yet not all selected retrievals yielded satisfying results. A few retrievals have extremely high values that are deemed unlikely to occur, while others yield poor fits and high values for the mean statistical variation of the residual spectra (reduced χ^2). The χ^2 thus corresponds to the misfit between measured and modelled spectra for the best-fit water vapor abundance.

The aforementioned benefit of an increased DOF by the use of a spectral synergy approach is demonstrated in Figure 3. While water vapor column abundances from all available co-located

observations were shown in Figure 2, only data points with a reduced χ^2 of the retrieval equal to or smaller than 4 are shown in Figure 3, where the distribution of abundance-to-noise ratios (ANR) and the DOFs for the synergy are shown along with the parameters from SPICAM/NIR and PFS/TIR. The ANR, as the retrieved water vapor column abundance devided by the a posteriori error, provides a measure of the amount of certainty one can have in the output value. Note that for visibility reasons, the data points are layered according to method, such that PFS and SPICAM data points overprint those of the synergy.

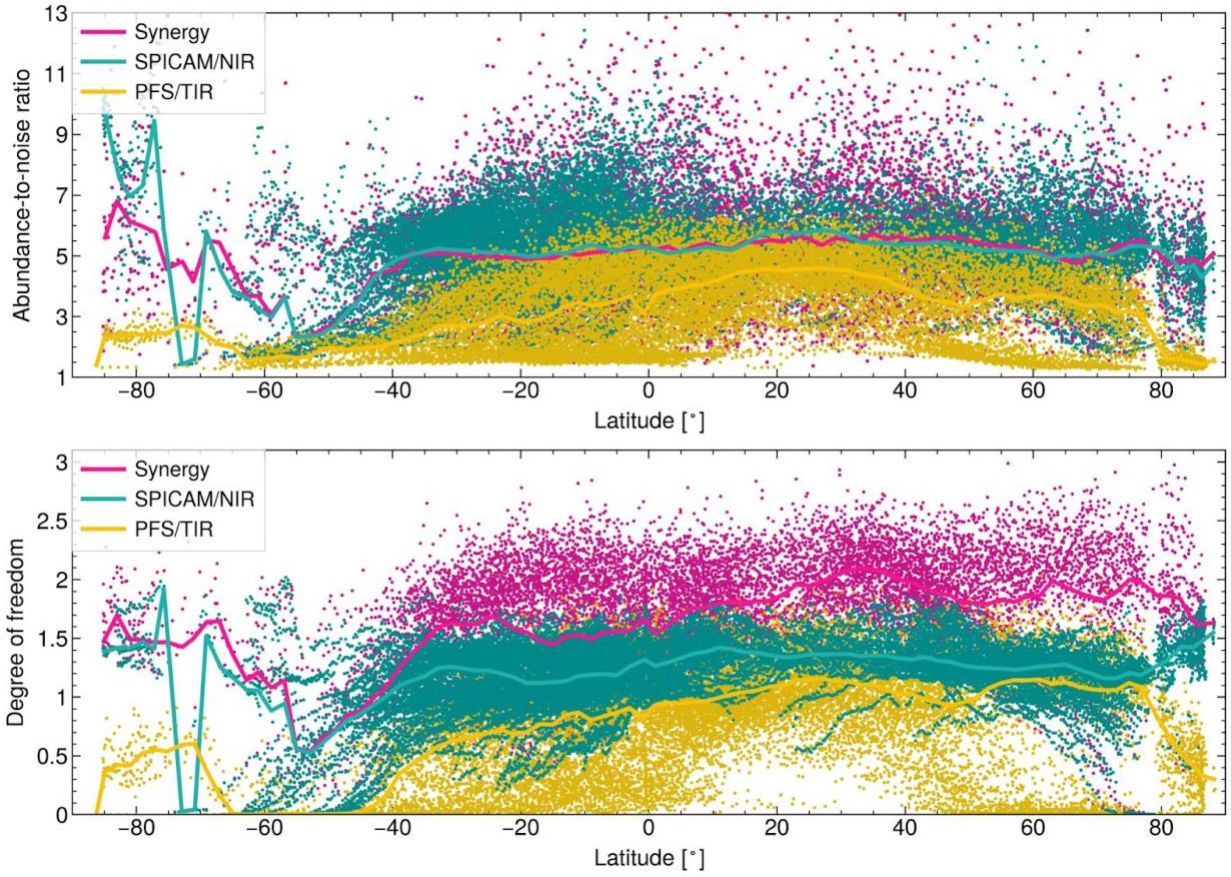

Figure 3: Abundance-to-noise ratio and degree of freedom from the synergy and the single spectral domain retrievals. Dataset is limited to those retrievals which satisfy the criteria of a reduced χ^2 equal to or smaller than 4 and an ANR equal to or larger than 1 in MY 27. Top panel: ANR for the synergy, PFS and SPICAM retrievals. Bottom panel: DOF for the synergy, PFS and SPICAM retrievals. Data points are layered, with the synergistic points at the bottom. Solid lines represent averages binned in intervals of 2° Ls.

The ANR values are shown as scattered dots for each individual retrieval, and the solid curves represent binned averages of 2° Ls. The selected data are limited to all retrievals with ANR >=1 to ensure the presence of water vapor, as it corresponds to a 1-sigma detection limit. The synergy and SPICAM have very similar ANR distributions, both averaging at around ANR=5, with the synergy only occasionally outperforming SPICAM mostly at mid latitudes, showing that the synergy provides highly robust column abundances. PFS/TIR displays the smallest spread in

ANR, covering the range from ~1.5-6 and with an average of around 4. SPICAM/NIR retrievals mostly range between 2 and 8 and remain above 4 for all latitudes north of -40°N.

The DOFs for each method is shown in the bottom panel of Figure 3, where the notable increase in DOF for the synergy verifies that the water content along the vertical can be roughly resolved. The DOF fluctuates around 1.0 for the NIR and TIR single spectral domain retrievals, while it typically exceeds 1.25 for the synergy, fluctuating around 1.5. Note that the spread in DOF values is small for NIR compared to TIR, and that NIR regularly achieves DOFs around 1.5, higher than what is ever obtained with TIR. In the southern hemisphere and near the north pole, the TIR DOFs nearly never exceed 1, while the synergy remains stable and high in the north polar region especially, but also performs reasonably well in the south. With a DOF consistently higher than one, the synergy is capable of providing information on the shape of the profile, and a vertical partitioning can be obtained.

The synergy returns a vertical profile and an integrated column abundance for each co-located observation. To ensure the synergy is not simply reproducing the a priori when retrieving a vertical profile and to demonstrate that the synergy is capable of distinguishing near-surface water vapor from the rest of the column, we quantified the amount of synergistically added information, compared to the MCD a priori profile, by altitude as a function of latitude and season. The ratio of the post-to-prior errors are visualized in Figure 4, where each panel represents an altitude indicated by the number on the left y-axis. Within each panel, data are binned by 2° in Ls and 2° in latitude. At higher altitudes, the error ratio is fairly close to one, meaning that the synergy brings little new information. However, deeper in the atmosphere, more information is progressively added by the synergy. The panels representing the atmosphere at 2.5-7.5 km are the altitude regions where most information is injected, and which benefits the most from the synergistic approach as was also evident from the single example in Figure 1. The retrieved profiles could be deviating from the MCD, which we will investigate further in Section 4.2, but the water mixing ratios are significantly more constrained, as also demonstrated in Figure 1.

In order to only select retrievals which are robust enough to justify a deeper analysis, and with a high enough quality that information on the vertical water distribution can be extracted, four criteria were established which the retained samples would have to comply with simultaneously: i) an ANR ≥ 3 (3-sigma detection limit), ii) a DOF for water vapor ≥ 1.25, iii) a post-to-prior error ratio ≤ 0.9 for water volume mixing ratio at 2.5 km (Error ratio), iv) a reduced χ^2 of the retrieval (Chi2) $\leq$ 4. Many criteria limits were explored to optimize the returned number of retrievals versus the quality of said retrievals. The limits of these criteria can also be tailored for a specific purpose; the DOF limit was reduced to 1 for the assembly of a composite column abundance climatology.

A visualization of the statistical distribution of the relative numbers (per 10 000) and combinations of fulfilled criteria is shown in Figure 5. The first panel of Figure 5 shows the distribution of fulfilled criteria when the synergistic retrieval method is used. The second and third panels visualize the relative numbers and distributions of fulfilled criteria when only the NIR and TIR spectral intervals are utilized.

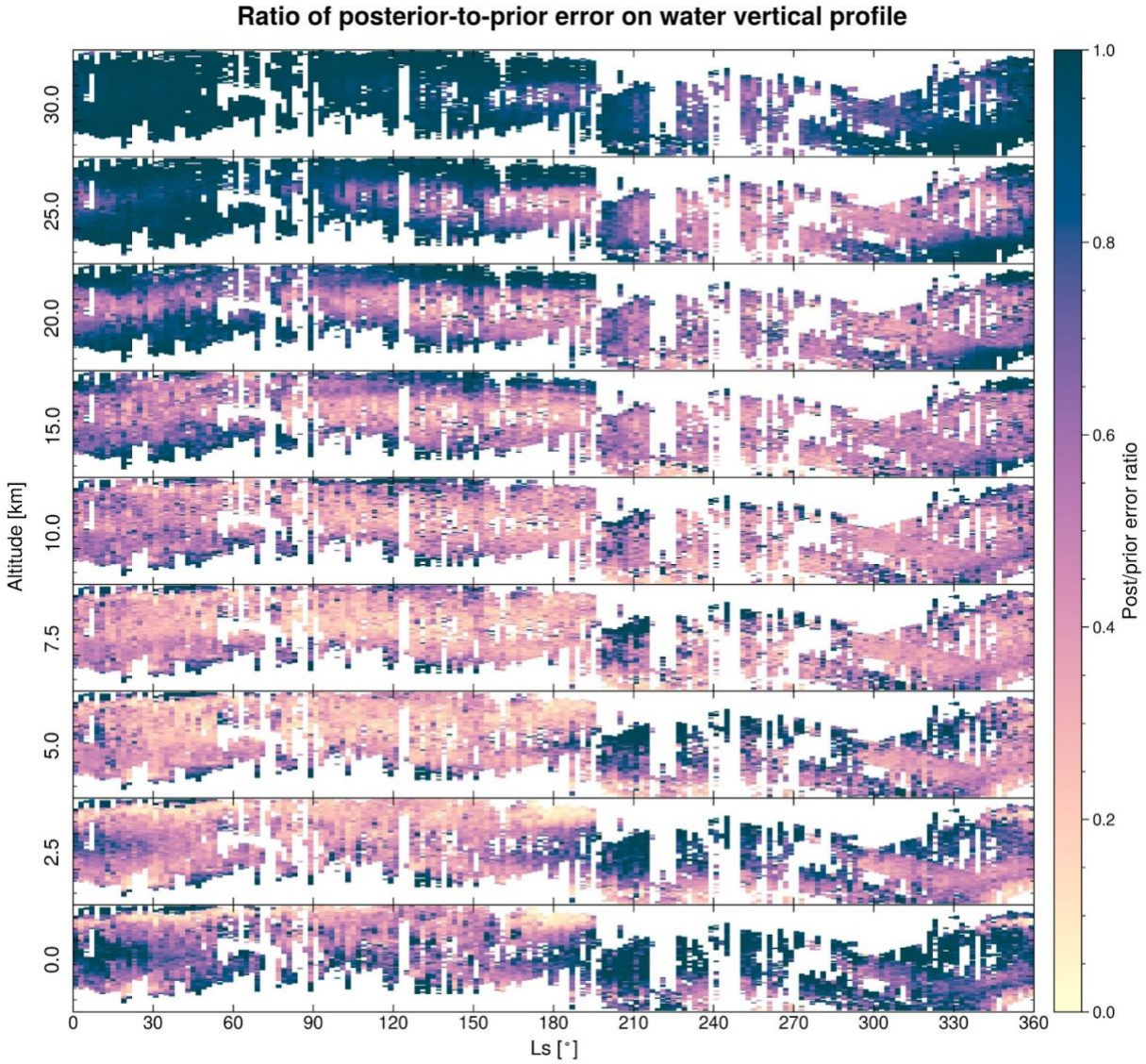

Figure 4: Illustration of the benefit of utilising the synergistic retrieval by altitude, latitude and season. Each panel represents an altitude level, with the given altitude in km given on the left. Within each panel, the y-axis represents latitude, with major ticks every 30°. Data were averaged in bins of 2° latitude and 2° Ls. The retrieved a posteriori errors are divided by the MCD a priori error profile, such that values below 1 represent retrievals where the uncertainty has been reduced, and thus the co-located observation has injected additional information into the retrieval process.

The benefits of using two spectral ranges is clearly visible, with more than 55% of all synergy retrievals fulfilling all criteria compared to only 24% for SPICAM/NIR, and 16% for PFS/TIR, effectively demonstrating that the synergy yields more information than separately using the SPICAM or the PFS dataset. For all cases the χ^2 is the most restrictive requirement (except for PFS/TIR where the DOF is the most restrictive), while the ANR is the least restrictive. The DOF increase provided by synergy compared to retrievals from single spectral domains is a direct

evaluation of how much additional information synergy brings to constrain water vapor distribution. Only the measurements fulfilling all four requirements are considered in the following analysis.

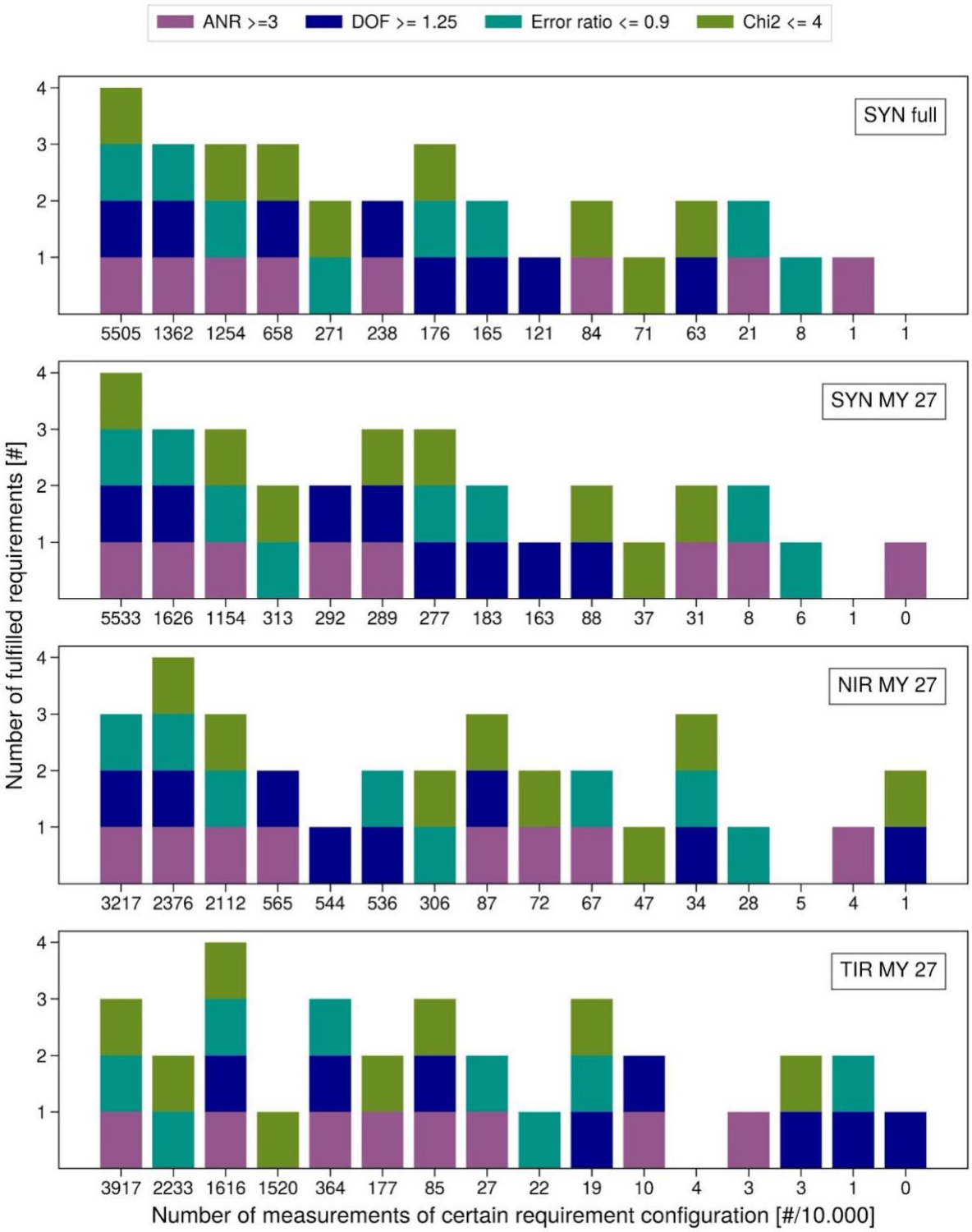

Figure 5: Overview of the relative statistical distributions of fulfilled criteria. The full synergy dataset is shown in the top panel, the synergetic retrievals in MY 27 in the second, SPICAM/NIR is shown in the third panel, while PFS/TIR is illustrated in the bottom panel. Retrievals with the individual instruments were only conducted for MY 27. The y-axis counts the number of fulfilled criteria, and the x-axis shows the number of retrievals per 10 000 which fulfill each criterium configuration, sorted with the most likely configuration to the left, and decreasingly likely configurations towards the right.

4 Results

The results presented below were derived using data from two time intervals; Ls=334 of MY 26 until the end of MY 29, and from the beginning of MY 32 to the end of MY 34. The spatial and temporal coverage within each year is highly variable. All four selection criteria described in section 3.2 were applied, with limits as shown in Figure 5 (except for the assembly of the column abundance climatology in section 4.1, which uses limits specifically adjusted for column abundances). The first part of this section focuses on the retrieval of total column abundances with the synergy compared to with single spectral domain approaches and to the MCD. Then, results concerning the vertical partitioning of water is shown, as seen in relation to the total column and model predictions, where special attention is given to the polar regions around the seasonal ice cap sublimation seasons.

4.1 Column abundance climatology

For the assembly of a complete and composite synergy climatology of water vapor, the criteria described in Section 3 are applied to the complete dataset shown in Figure 2, with an adjustment to the DOF and error ratio limits. The DOF and error ratio requirements ensure retrievals with sufficient vertical information to justify further analysis of partitioning, and as there is no need for vertical information content for a column abundance climatology, the DOF and error ration limits are both set to 1, which is more than sufficient to infer a highly reliable column abundance.

After the adjusted selection criteria are applied, the remaining water vapor retrievals are illustrated as a function of season, latitude and longitude in Figure 6. In order to account for topography, the total water columns are normalized to an equivalent surface pressure of 610 Pa using the MCD to constrain local pressure. However, this pressure normalization is made on the assumption that water vapor is well mixed with the ambient gases, which might not always be the case. The total water columns are averaged in bins of 2° Ls, 2° latitude and 4° longitude. Of all qualified retrievals, 31% are from MY 27, which for the most part contributes to the coverage of the northern summer.

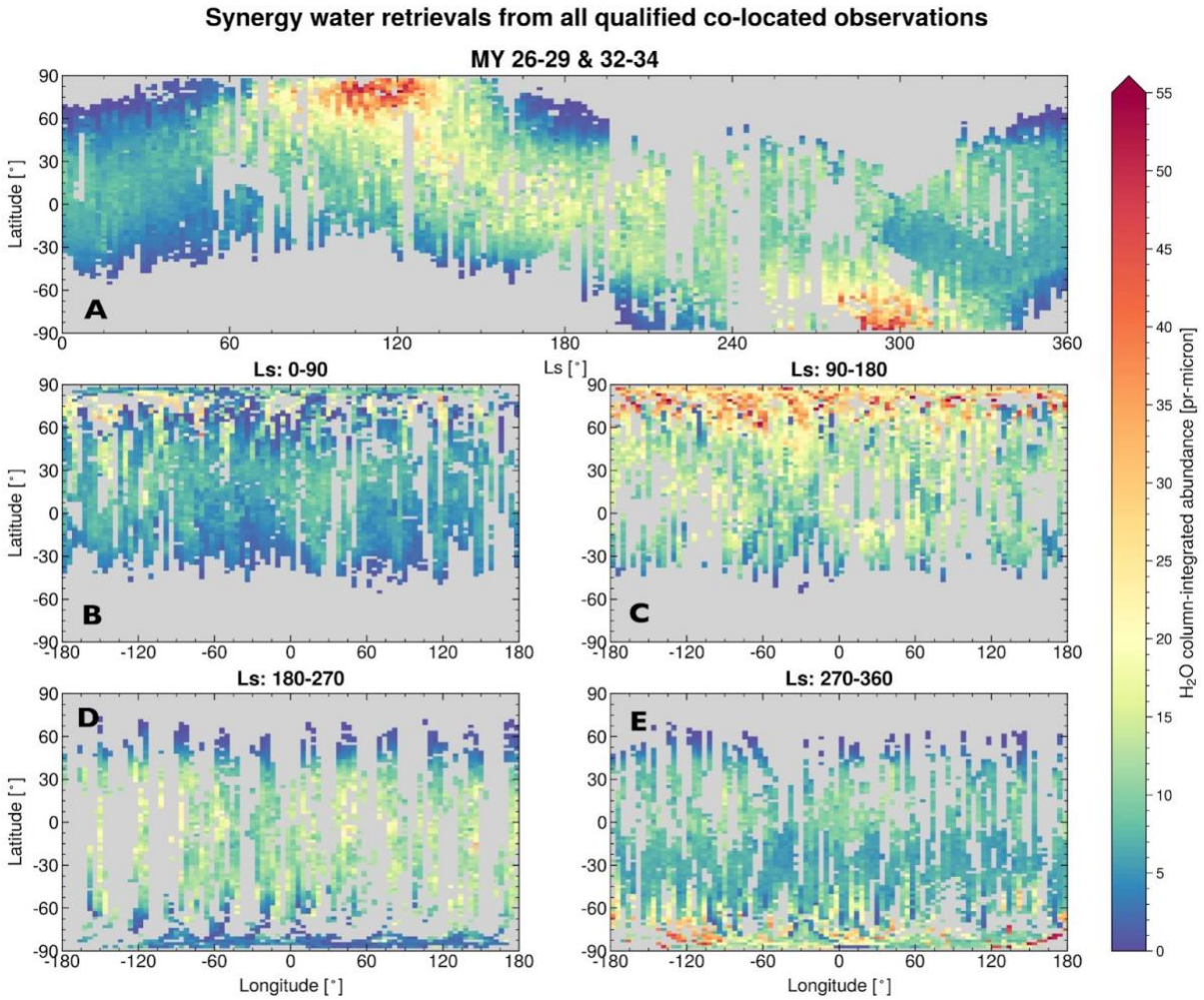

Figure 6: Seasonal and geographical variations in normalized total column abundances of water vapor. Panel A: Seasonal distribution of all qualified retrievals averaged in bins of 2°x2° Ls and latitude. Panels B-E: Geographical distribution of qualified retrievals for each seasonal interval, averaged in bins of 2°x4° latitude and longitude.

Given the variation of the sampled local times (from early morning to late evening for SPICAM and from 08:00-16:00 for PFS), it is assumed that seasonal variations of water vapor column abundances dominate over any diurnal variability. Although the temporal and spatial coverage is incomplete, known trends of the water cycle appear unambiguously. The spring is overall a dry season (Figure 6 panel B), with abundances rarely higher than 10 pr-μm. The few instances with larger CIA occur late in northern spring at the edge of the NPC. The early northern summer season (Ls = 90° –135°) is characterized by large latitudinal contrasts with high water content in the polar regions which decrease monotonically southward, this is particularly prominent in Panel C. At around Ls=115°, a Northern maximum of ~60 pr-μm is visible poleward of 70°N, while at the same time only around 13 pr-μm is measured south of 30°N (in panel A). The northern hemisphere fall season shown in panel D displays a north polar region now devoid of water vapor, most of which having been transported to the mid and low latitudes and across the equator. The south polar maximum occurs around Ls=285° and reaches an average total column

abundance of 40 pr-μm, as seen in Figure 6 panel E. A global dust storm occurred in MY 28, which degraded the quality of the measurements for some time, causing the number of qualified retrievals in MY 28 to be low even though many observations were conducted in this period. The drier patch around Ls=300° in the southern hemisphere is constructed almost entirely from observations in MY 28, when the dust storm is thought to aid transport of water vapor from the lower atmosphere to higher altitudes (Fedorova et al., 2018).

4.2 Synergy compared to single domain retrievals and MCD

Numerous studies of the climatology of water vapor have been made using the PFS and SPICAM instruments individually. As this is the first time observations from both are used in synergy, a direct comparison has been made between them and the MCD. In Figure 7, synergy retrievals and MCD a priori values satisfying the adjusted criteria as described in Section 4.1 are plotted, along with single spectral domain retrievals for SPICAM and PFS. No criteria have been imposed on the single domain retrievals other than unphysically high abundances have been filtered out. CIAs are averaged across the 15°-45°N latitude band, the region which contains the longest continuous coverage, and in intervals of 5° Ls.

The selected time period covers the early northern summer, the polar cap sublimation season and continues into late summer of MY 27. In general, the MCD predicts a much higher water vapor abundance than what is obtained with either of the retrieval approaches (except during Ls=120°-140°). The MCD agrees well with the observations only at the very beginning and end of the time period shown here, which corresponds to before the onset of the sublimation season, and after the water vapor has been transported beyond the area of focus. This might suggest that the transportation mechanisms dominant in the summer mid-latitudes are currently not fully understood. Another factor which could impact this discrepancy is the large MCD sublimation peak, which might then propagate southward. The difference in the CIA, as well as the vertical partitioning, predicted by the MCD and the values retrieved by the synergy are further elaborated upon in section 4.3.

The synergy and the single spectral domain retrievals with PFS/TIR are overall in good agreement, with the synergy yielding similar or slightly lower. SPICAM/NIR also agrees well with the synergy and PFS, albeit with slightly larger abundances. The difference in abundances have been suggested to be related to effects in different spectral bands used and specific retrieval methods (Korablev et al., 2006; Maltagliati, Titov, et al., 2011). The general seasonal behavior displayed by the three retrieval approaches is similar; an increasing trend in the early summer, peaking at around Ls=135°, when water vapor from the North Polar Cap (NPC) has sublimed and been transported to mid-latitudes. The MCD predicts a much more rapid increase of the sublimed water, with CIA values a factor of 2.5 higher than the synergy at Ls=100°. The decreasing CIA found after Ls=140° by both the synergy and the single spectral domain retrievals as well as the MCD is expected, as the water is successively transported across the equator. The “double-hump” shape of the MCD abundances (also evident in Figure 10) are not clearly distinguishable from either the retrieval techniques.

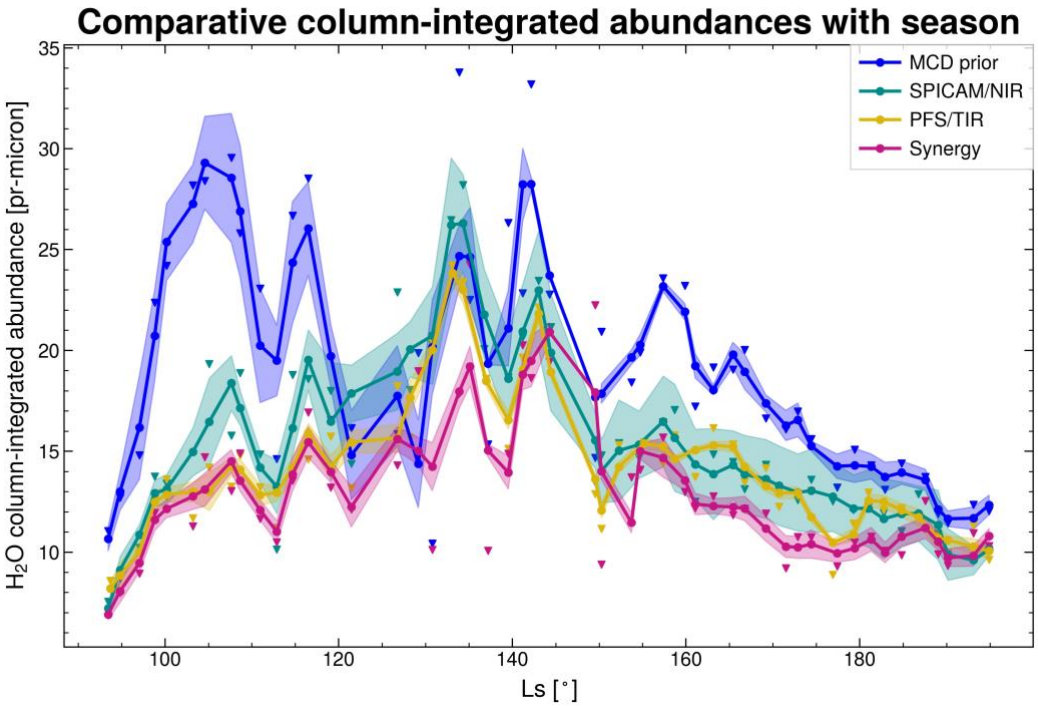

Figure 7: Seasonal evolution of column-integrated abundances of water vapor during summer of MY 27. Comparison between abundances predicted by the MCD used as a priori, the synergistic retrievals and the single spectral domain approaches for SPICAM and PFS. Abundances are not normalized to an equivalent surface pressure. Data are averaged on the latitude interval 15°-45°, and in bins of 5° Ls. Triangles represent the average values for each bin, the solid curves are the smoothed abundance values, and the shaded areas represent the standard error for each bin average.

4.3 Vertical partitioning of water vapor

The spectral synergy method produces vertical profiles of water vapor where the data points are higly correlated. Even though the synergy significantly increases the DOF of the water vapor retrieval, it is still too low to provide a true profile with individual mixing ratios. The points along the vertical profile are highly correlated, as the DOF is usually around 1.5. Figure 8 shows a selection of example profiles from specific regions and seasons of interest. Light hues are individual profiles, with the dark blue and black being the mean profiles from the synergy and MCD respectively. The three example periods are from left to right: NH low latitude late spring, NH mid latitude early summer and SH mid latitude mid summer. For all three examples, the synergy obtained a higher PI, especially so for the NH early spring. The MCD profiles are most often fairly constant, with a very stable water mixing ratio with altitude. The exception is at low latitudes in NH early spring, when the MCD indicates the presence of a wet layer peaking at 10 km. The synergy also finds somewhat elevated vapor amounts here, but peaks instead near the surface at 2.5 km. In all cases the water vapor does not appear evenly mixed below the boundary layer, and shows a clear tendency for a strong near-surface water confinement.

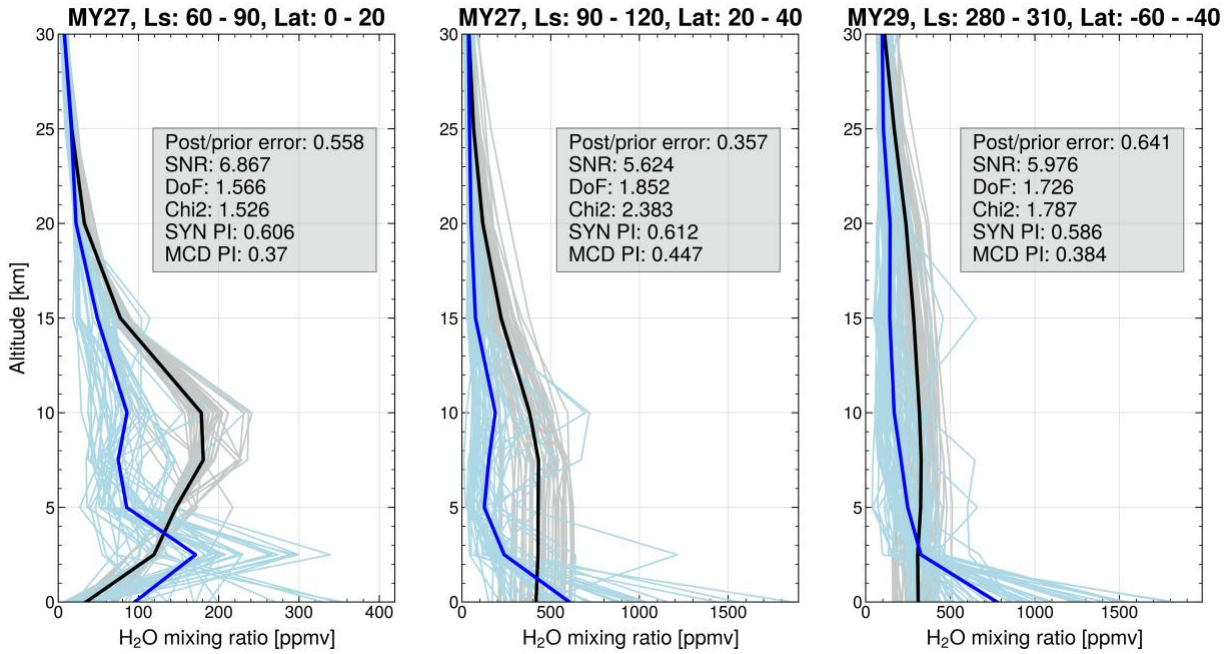

Figure 8: Selection of synergy and MCD a priori vertical profiles of water vapor. Light blues and greys are individual profiles, while dark blue and black are mean profiles. The three example periods are from left to right: NH low latitude late spring, NH mid latitude early summer and SH mid latitude mid summer. The text boxes give the mean numerical values for the four selection criteria along with the a posteriori and a priori partitioning index values.

When water vapor is retrieved simultaneously from PFS/TIR and SPICAM/NIR, the degree of vertical confinement can be estimated by taking the ratio of the partial column from the surface up to 5 km, to the total column. The result is a dimensionless partitioning index (PI) representing the amount of water vapor confined within the first 5 km of the atmosphere compared to the rest. Average trends in the CIA and PI during the northern summer (Ls=90-200) are shown in Figure 9, with focus on the latitudes between 45°S and the North Pole where the observation density is highest.

As the seasonal polar ice is subliming in early northern summer, the CIA increases drastically north of 60°N. There is no clear immediate reaction in the PI, which is fairly high (PI typically greater than 0.7) and stable from 30°N and northward during Ls=90°-160°. At polar latitudes between Ls=100°-130°, when the CIA is at its highest, a local PI maximum is observed slightly southward of the CIA maximum. The confinement in the polar region remains strong at least until Ls=170°, a period during which latitudes above 50°N undergo extreme variations in CIA, transitioning from the north polar summer maximum to a very dry late summer, as can be seen from the top panels in Figure 9. Extremely strong partitioning (PI=0.9) is seen at Ls=165°, when almost no water remains in the far north. This indicates that after most of the water has sublimed and been transported south, what water vapor remains at high latitudes is kept close to the surface for the duration of the summer.

South of the equator the water vapor is more homogeneously distributed with altitude with a PI of around 0.5, with some regions at low latitudes showing signs of a drier boundary layer (PI ~0.2). The PI is highly variable and related to topography in an anticorrelated fashion when

compared to the CIA. Even after pressure normalization, there are local variations in CIA related to varying elevation, previously found to likely be linked to atmospheric dynamics (Fouchet et al., 2007). Geographical variations stand out in the bottom panels, where the PI is enhanced over drier, elevated regions such as the Tharsis and Terra Sabaea regions (centered around -120° and 30° longitude respectively), while the confinement is small over low-elevation regions such as Hellas Planitia at longitudes between 60°-90°. The PI index is a ratio of water columns, and should inherently be independent of topography, yet the correlation with elevation remains.

PIs smaller than 0.5 are rarely seen in the NH, suggesting that sublimed water vapor might be transported southward at low altitudes. At low latitudes however, the water is transported across the equator over regions of low elevations

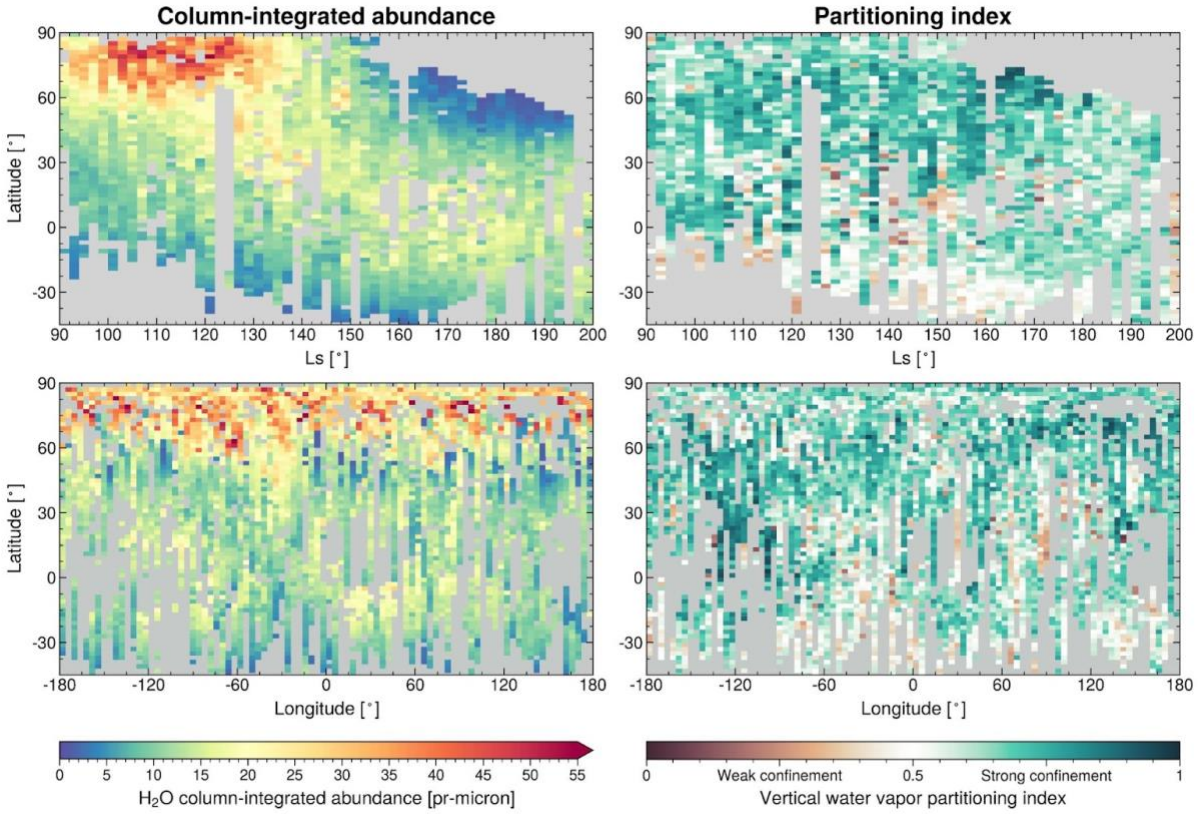

Figure 9: Composite maps of normalized water vapor column-integrated abundance and partitioning index. For the partitioning index, values higher than 0.5 (in green) indicate that more than 50% of the water vapor column is confined below 5 km, while lower values (in brown) indicate that water vapor is more evenly dispersed with altitude. Data from all available years fulfilling all requirements have been averaged in bins of 2° latitude, 2° Ls and 4° longitude.

4.4 Deviations from the MCD

The synergistically retrieved column abundances and vertical confinement shown in Figure 9 contain significant differences from the MCD a priori estimates. Figure 10 illustrates the deviations of these synergistic values from the MCD estimates as a relative difference with the MCD abundances as reference values ($rel.diff. = \frac{SYN-MCD}{MCD}$) , such that a deviation of 0 means the synergy and the MCD are equal, and instances where the synergy gives the larger values are

positive. The relationship between the retrieved and a priori CIA is shown in the left column, and of the retrieved and a priori PI in the right column.

Figure 10 shows that, on the whole, the synergy has a tendency to retrieve column abundances lower than the corresponding MCD a priori values. The sublimation peak in early summer (around Ls=110°), which controls most of the total atmospheric water vapor throughout the year on the whole planet, is significantly smaller than the MCD estimate, yet agrees somewhat better with the MCD than the surrounding observations. The total water content in the tropical fall is a good indicator of meridional transport of vapor from northern polar regions (Navarro et al., 2014), and this is where the model and synergy are most similar.

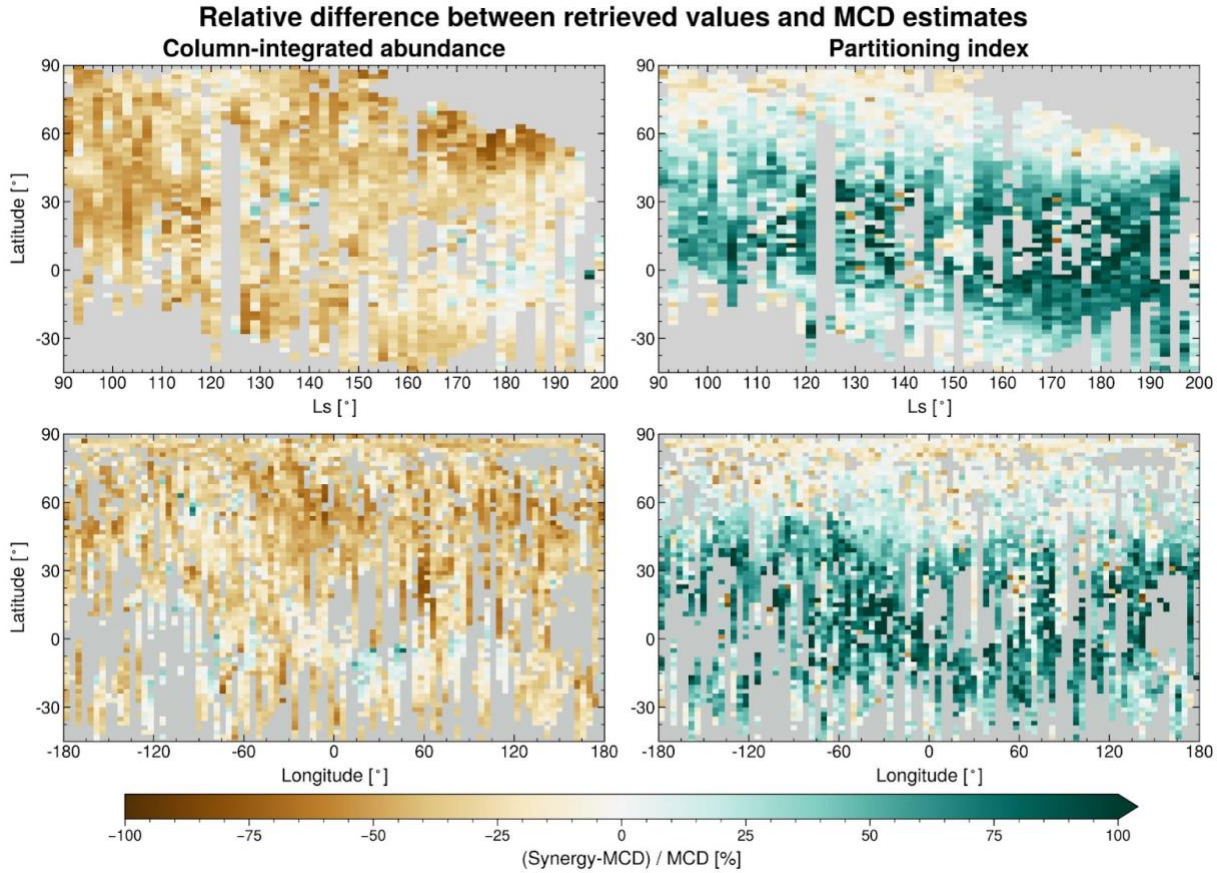

Figure 10: Illustration of the relationship between the retrieved values and the MCD a priori. The deviarion of the synergy from the MCD estimates are calculated as a relative difference such that a value of 0 indicates where the synergy and the MCD are equal, and instances where the synergy yields larger values are positive. The left column shows the ratio of the a posteriori to the a priori full water vapor column, while the right column shows the ratio of the a posteriori to the a priori partitioning indices. The top row visualizes the data on a latitude by Ls grid, while the bottom row distributes the data on a latitude-longitude map. Data from all available years fulfilling all requirements has been averaged in bins of 2° latitude, 2° Ls and 4° longitude.

The vertical confinement displays the opposite behavior, with the synergy often finding a PI comparable to the MCD at mid and high latitudes. Note that during the sublimation season the

MCD quite accurately reproduces the observations, indicating that the sublimation processes of the NPC are quite well understood in terms of vertical distribution. The PI difference is highest at low and middle latitudes in late summer, when large amounts of water vapor are being transported from the NH and across the equator. At most, the synergy PI at low-latitudes in late summer is almost twice as strong as model predictions. This is in general a fairly dry area, with a CIA of 10-15 pr-μm, where the synergy indicates that roughly 60% of the column is confined below 5 km. The atmospheric behavior in this region is less dominated by temperature and more affected by wind. The details of local air flow patterns are typically known with less certainty than temperature variations, which could explain why the model deviates the most from the observations at low and mid-latitudes.

4.5 Seasonal evolution of water distribution with latitude

The seasonal variations of the CIA and PI can be visualized by zonal averages plotted as a function of latitude. All data points in Figures 10 and 11 illustrate the CIA and PI averaged in bins of 2° latitude and 15° intervals of Ls, and the curves are smoothed using a Savitzky-Golay low-pass filter with a second order polynomial and a window corresponding to 20° latitude. Curves covering the same seasonal periods have identical colors for both hemispheres to aid cross-hemispherical comparison (for example, the red curve corresponds to mid-spring for both hemispheres; Ls=45°-60° in the NH and Ls=225°-240° in the SH).

Both hemispheres are fairly dry from the equator to mid-latitudes during the spring-summer season. The SH displays a smaller spread in seasonal variation and a smaller increase with latitude compared to the NH, remaining at around 10 pr-μm from the equator to 40°S. From there, the water column starts to increase steadily. Overall, the synergy and MCD agree very well in the SH, with the most noticable difference being the degree of seasonal spread, distinguishable at all latitudes in the synergy, while only becoming distinguishable after 40°S for the MCD. All synergistically retrieved seasonal curves show a southern maximum which is migrating poleward with season, matched well by the MCD. The exception is the first seasonal average in mid-spring (Ls=225°-240°) which displays a continuously decreasing curve, with the highest value at equator for the synergy, while the MCD finds a weak maximum of 15 pr-μm at 70°S for the same season. The SH sublimation season maximum occurs during Ls=285°-300°, with a maximum value of 34 pr-μm near 87°S.

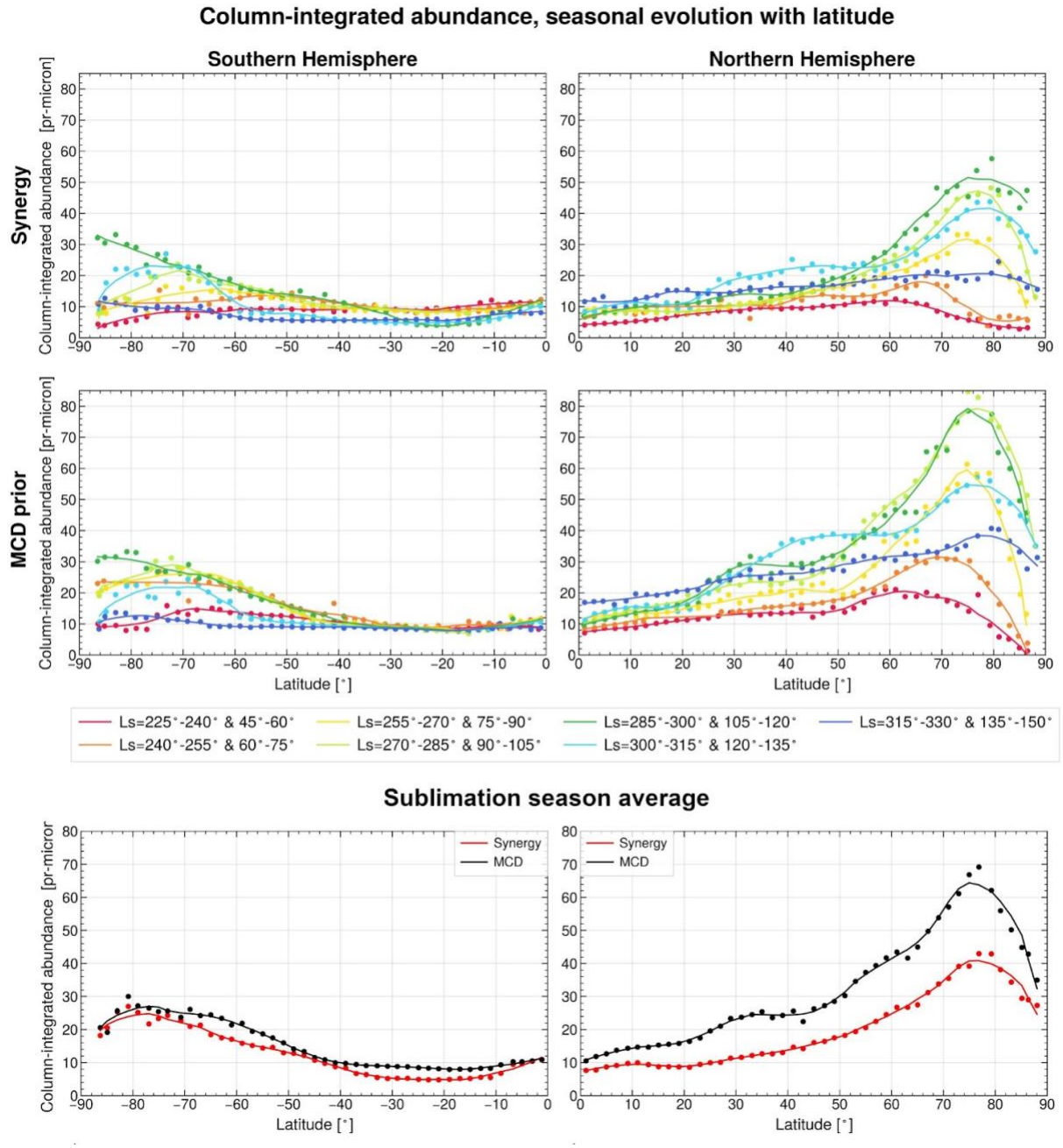

Figure 11: Zonal averages of water vapor column abundances from mid-spring to mid-summer for both hemispheres. The top four panels show column abundances for all years, the dots are data points averaged in bins of 2° latitude and 15° Ls, while the curves represent the smoothed bins. The top row illustrates the synergistic retrievals, while the middle row shows the corresponding MCD a priori column abundances for each hemisphere. Curves representing the same seasonal period for both hemispheres have identical colors, with the SH Ls interval listed first. The two bottom panels compare the synergy and the MCD averages from Ls=255°-315° for the SH and Ls=75°-135° for the NH, covering the sublimation season for both hemispheres.

The MCD shows a decreasing trend for all seasons in the extreme high latitudes poleward of the CIA peak, as expected due to the polar cap circulation known as the polar cap breeze (Haberle &

Jakosky, 1990), the Martian equivalent to the terrestrial sea breeze. The effect is expected to be stronger in the NH where the more massive ice cap generates a larger temperature gradient. In the retrieved synergy data, the CIA does not always decrease poleward of the cap edge in the SH, and most noticeably continues to increase even beyond 80°S for observations during Ls=285°-300°. This could be due to averaging of data from multiple years (Pankine et al., (2010) reported high interannual variability of this behavior over the NPC), imperfect coverage of this region and season, or perhaps a variable polar cap breeze in mid-summer is not effectively transporting water vapor off the polar cap.

The NH is as expected far wetter than the SH. The CIA increases monotonically from the equator, and does not remain constant across large regions, as in the SH. Distinct maxima are visible with decreasing abundances northward of 80° latitude for all seasonal intervals, in agreement with the model. The overall maximum is observed at 80°N in the Ls=105°-120° interval, same as in the SH, and reaches a peak value of 60 pr-μm. The highest column abundance obtained by the MCD is in the interval Ls=90°-105° and reaches 83 pr-μm. The locations of the CIA peaks are found just south of the polar cap edge with a clear decreasing trend for all seasons in the extreme high latitudes poleward of the CIA maximum, as expected due to the effects of the polar cap breeze. The sublimation onset is observed to occur later than what is predicted from the MCD, where during Ls=60°-75°, the synergy finds a gradually increasing latitudinal trend with a modest peak at 65°N of just below 20 pr-μm, while the MCD already estimates a significant maximum of 30 pr-μm at 70°N.

In the bottom two panels of Figure 11, seasonal averages of the intervals Ls=255°-315° for the SH and Ls=75°-135° for the NH (covering the main sublimation period for both hemispheres) are shown to provide comparisons between the general trends in meridional CIA gradients from the synergy and MCD. The CIA absolute values are interesting to compare, but even more so the meridional variation. The summer sublimation maximum in the MCD is quite easily adjusted by tuning model parameters, while the change with latitude is subject to convection, transportation and possible surface exchanges, and not so straightforward to modify to obtain the desired output. In the south the trends are nearly identical, with the synergy only yielding slightly smaller average abundances in the 10°-30°S and 50°-70°S regions. In the north, the MCD deviates from the synergy most significantly in two places; at 20°N and at 50°N, where in both instances the MCD gradient distinctly increases with respect to the synergy. The “double-hump” shape of the CIA is also much more prominent in the MCD. The difference between the MCD and synergy is small towards the equator for both hemispheres, which might be indicative that the influence of the CIA sublimation peak diminishes at lower latitudes.

Seasonal differences in the PI appear small in the MCD model compared to observations, as can be seen for all seasons in Figure 12, where all the curves are more or less stacked on top of each other. In our retrievals the partitioning exhibits a wave-like behavior in both hemispheres, oscillating roughly around PI=0.5 in the south and around PI=0.65 in the north. The shape of the MCD PI curves resemble those of the CIA seasonal averages, and do not have the same wave-like quality that the synergy finds. As the synergy yields very stable column abundances, for low/mid latitudes for all seasons, the partitioning varies greatly, particularly in the southern mid summer. However, the number of data points in the SH are far fewer than for the NH, and the averages from this region should therefore be considered somewhat less precise. This disagreement is also visible (to a lesser extent) in the NH, indicating that the discord is likely not purely a result of poor sampling in the south. In the NH there is a clear tendency for the

partitioning to suddenly increase poleward of 80°N while the total water content decreases. The MCD PI on the other hand has been steadily increasing from the mid latitudes, and during late spring the PI even decreases north of 80°N. In the north, no stable PI gradient is observed as the MCD suggests. The synergy finds a highly variable PI for all latitudes and seasons, but with no clear meridional tendency.

These differences between the MCD and synergy are highlighted in the sublimation season averages for the PI in the two bottom panels of Figure 12, which clearly show the observed wave-like behavior being consistently higher than the estimated stable MCD PI. While the MCD indicates that around 40% of the water column is kept near the surface at all latitudes and seasons, the synergy finds that number to vary from 40-60%, with local maxima at equator, 50°S and at the pole. This trend is very similar to what is observed in the north, but here the wave amplitude is smaller. The MCD PI here is not as stable as in the south, and displays a fairly constantly increasing gradient from the mid latitudes (PI=0.4) towards the north pole (PI=0.75). The synergy finds that the PI seasonal averages never goes below 0.6, indicating that most of the column is always kept close to the surface. This leads to the synergy and MCD finding similar PI values only in the north polar region.

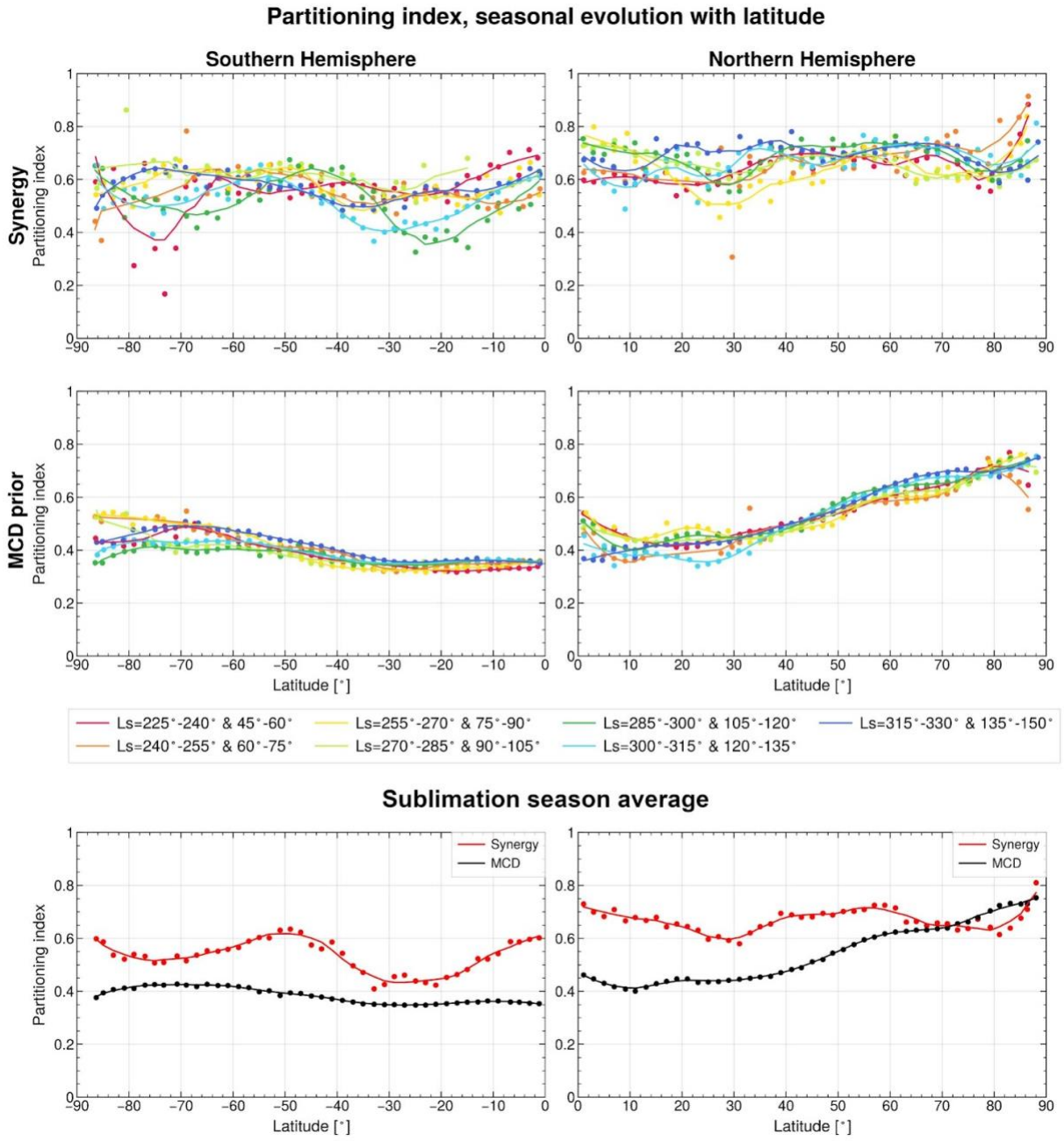

Figure 12: Zonal averages of the vertical partitioning index for each hemisphere from mid-spring to mid-summer. The top four panels show data for all years averaged in bins of 2° latitude and 15° Ls as dots, while the curves represent the smoothed bins. The top row illustrates the synergistically retrieved partitioning indices, while the middle row shows the corresponding MCD a priori indices. Curves representing the same seasonal period for both hemispheres have identical colors, with the SH Ls interval listed first.The two bottom panels compare the synergy and the MCD averages from Ls=255°-315° for the SH and Ls=75°-135° for the NH, covering the sublimation season for both hemispheres.

4.6 Closer look at the North Pole

The northern polar region in spring and summer is of particular interest as the sublimation of the seasonal NPC is the main source, and thus the main forcing, of the water cycle. Every summer, as the NPC is exposed to sunlight and its surface temperature increases, more than one Gigaton of water vapor is released into the atmosphere (Smith, 2002), spreading around the entire globe as the seasons unfold. Figure 13 shows the CIA and the vertical confinement in the form of polar plots to better visualize the spatial distribution of the observations. Data from all available years north of 45°N are averaged in seasonal intervals of 30° of Ls, and on a 1°x7° latitude-longitude grid. The two top rows of Figure 13 illustrate the CIA, and the two bottom rows show the PI. For each group the synergy values are followed by the MCD values.

Overall, the MCD predicts higher CIAs than the synergy (as also seen in Figure 10), with high abundances extending further equatorward, than what is observed. The sublimation season also appears to be initiated earlier in the MCD than what is observed, as can be seen by comparing the two first rows of the first column (Ls=60°-90°) of Figure 13, and was also shown in the previous section in Figure 11. At 75°N, the MCD finds column abundances higher than 40 pr-μm, when no observations for this time and place yield higher CIAs than 30 pr-μm. The situation is reversed for the vertical partitioning, where the synergy indicates a stronger near-surface confinement at all latitudes compared to the MCD. During Ls=90°-120°, the larger sublimation peak of the MCD is likely contributing to the overestimation of water vapor at mid-latitudes as seen in Figure 7. This was also shown in Figure 10, where the synergy is as much as 50% smaller than the MCD during Ls 90°-110°. For the late summer season 120°-150° Ls, the MCD predicts a high PI confined mainly to latitudes north of 60°, while the observations show a high PI reaching the mid-latitudes. Overall, the MCD predicts the largest PI poleward of 75°N, while the observations indicate that the PI remains high for all latitudes, albeit more variable (this was further explored in section 4.5). Still, the largest differences in the vertical confinement are found in the mid-latitudes and not in the polar regions, as illustrated in Figure 10.

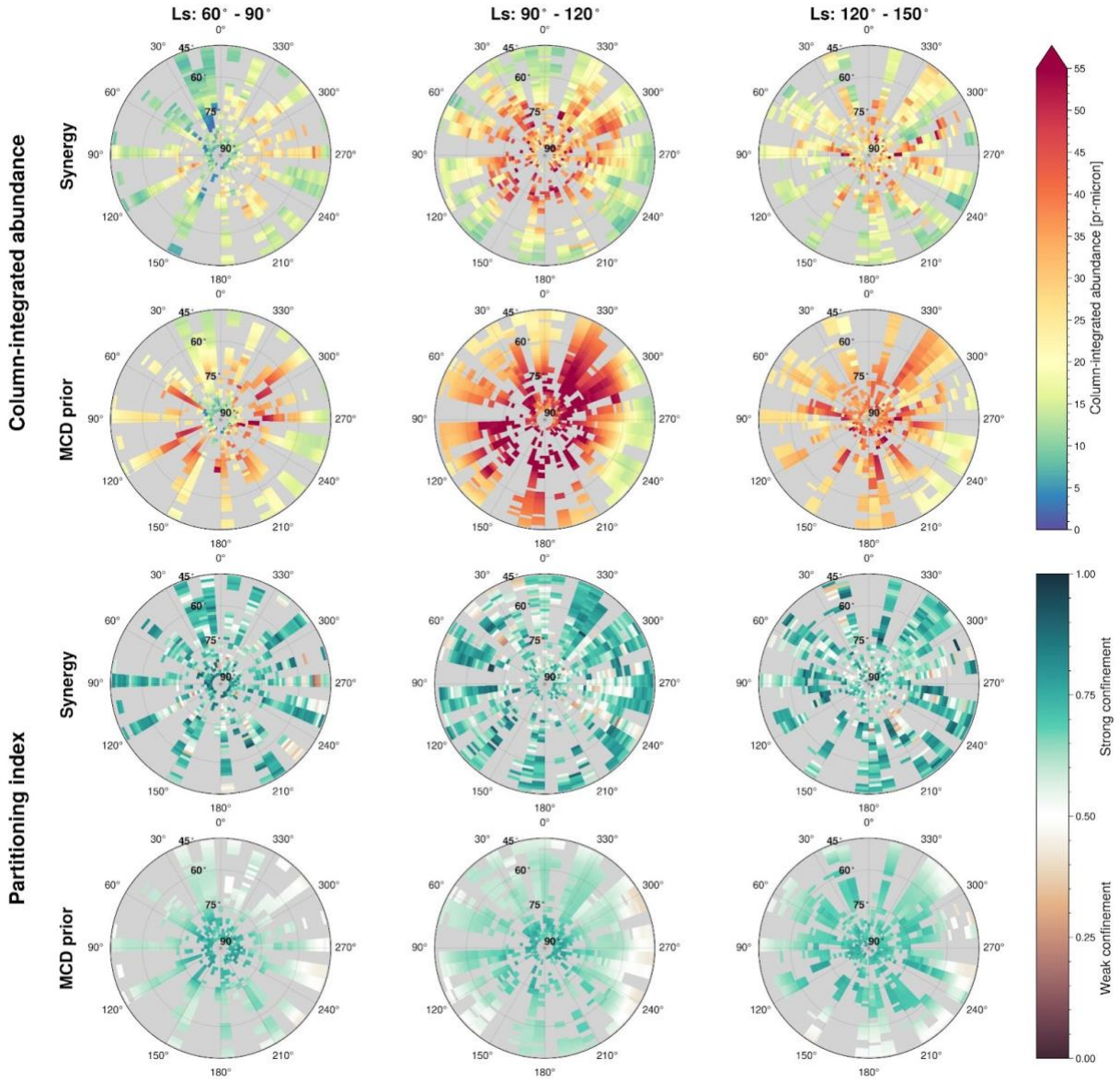

Figure 13: Polar view of the column-integrated water abundance and the partitioning index. Observations northward of 45° are averaged on a 1°x7° latitude-longitude grid, in intervals of 30° Ls. The top two rows show the full column abundance of the synergy retrieval (first row) and MCD a priori (second row). The bottom two rows show the retrieved partitioning index (third row) and the MCD a priori partitioning index (bottom row). A higher partitioning index indicates that more water kept close to the surface.

5 Discussion

5.1 Column abundance

In this work, the MCD was used to provide a priori values for the column abundance retrievals with the uncertainty set equal to the abundance. With a post-to-prior error ratio analysis, we demonstrated that the synergy injects a significant amount of information to the retrieval, and obtains highly robust column abundances. The climatology presented here displays a water vapor

cycle consistent with established literature, both in terms of magnitude and seasonal and meridional variations. Water column abundances peak in early summer near the seasonal frost cap edge, where the vapor encircles and trails the retreating ice. It has been previously modeled (Houben et al., 1997), and more recently observed (Bibring et al., 2005; Kieffer & Titus, 2001), that water vapor subliming from the seasonal water frost annulus re-condenses on the surface of the retreating CO_2 cap, which explains this behaviour. The water decrease poleward of the annulus is observed consistently for all seasonal intervals, yet annual variations have been previously reported (Pankine et al., 2010), and are not discernible in in the composite averages presented here.

Although the overall behavior is well known and the trend agrees well with the MCD model, significant differences do exist. The synergy column abundances deviate most prominently from the MCD in terms of absolute value with significantly lower abundances, particularly in the summer NH. The observed northern sublimation maximum is 30% lower than MCD estimates, and the sublimation season onset itself is observed to occur later in time. The discrepencies between measuremens and the MCD have also previously been noted. The NH difference between synergy and MCD is very similar to the difference found by Savijärvi et al. (2019), where the MCD had to be scaled by a factor of 0.38 to agree with the local ChemCam data. When investigating the conditions at Jezero crater, Pla-García et. al., (2020) also found that the CIA peak reached Jezero crater sooner and was higher in the MCD compared to TES measurements.

In the SH, the model and observations are in better agreement, and similar to what was reported by Clancy et al. (2017) using CRISM occultation data, who also found that retrieved water vapor abundances matched MCD model estimates better in the SH than in the NH. The synergy yields slightly higher values in the southern early summer, resulting in a somewhat asymmetrical relationship between the synergy and MCD, where the synergy finds a lower summer peak in the NH, but a larger peak in the SH.

When compared to previous works, the synergy northern maximum abundance was quite consistent with PFS, SPICAM and the revised TES abundances of 60-70 pr-μm (Fouchet et al., 2007; Pankine et al., 2010; Trokhimovskiy et al., 2015), while with CRISM a slightly lower sublimation peak was obtained in MY 28 and 29 of around 50 pr-μm (Smith et al., 2009). Although the synergy finds a smoothed average of around 50 pr-μm at 75°N and Ls=105°-120°, some local and transient instances of abundances up to 100 pr-μm occur. Observations from the Limb and Nadir Observation channel of the NOMAD instrument on the ExoMars TGO satellite agree well with the synergy in terms of seasonal variations, however, the northern maximum obtained by the synergy is significantly higher than those found by NOMAD for the corresponding time and place (just above 30 pr-μm) (Crismani et al., 2020).

The southern maximum coincides in time with previous results, but the large asymmetry between the NH and SH maxima observed by SPICAM and CRISM is not as prominent in the synergy dataset (see Figure 6, where a few very high column abundances are observed), as the northern maximum is normally a factor of 2 higher than the southern peak for the corresponding season (Figure 11). On average, the synergy finds a southern maximum of ∼33 pr-μm, significantly higher than SPICAM. It should be noted that the location where the largest SH abundances were observed were at latitudes not captured by previous TES and PFS studies. It should also be pointed out that observations in the south polar region are much sparser than elsewhere, and measurements from several years are binned together, whereas the observations of the north

polar region are abundant and mostly from MY 27. Smith (2004) found that the year-to-year variations can be as high as 10 pr-μm, and might thus explain why we observe instances of high vapor abundances in the south.

Outside the summer maximums, the synergy again is most similar to SPICAM and PFS, and agrees very well also with NOMAD. During Ls=0°-50°, the mean low latitude (0°-30°N) CIA was 7-8 pr-μm for the synergy, SPICAM, PFS and NOMAD, and ~5 pr-μm for CRISM. Later, during Ls=150°-180° for the same latitudes, the mean abundances were 13-15 pr-μm for the synergy, SPICAM, NOMAD and CRISM, ~12 pr-μm for PFS.

The difference between the synergy and other datasets is most likely due to differences in calibration and data processing techniques, even though diurnal variations cannot be excluded. For example, NOMAD samples local times from 08:00 to 16:00, and PFS covers local times from morning into the late afternoon. TES sampled the equatorial region and mid latitudes around 14:00 and 02:00, with only data captured during the 10:00-14:00 range being used to assemble the revised dataset presented by Pankine et al. (2010). No evidence supporting diurnal variations have yet been uncovered using OMEGA or SPICAM (Maltagliati, Montmessin, et al., 2011; Trokhimovskiy et al., 2015), and in the synergy, any diurnal variations are lost in the averaging process as PFS and SPICAM cover a broader time interval. Crismani et al. (2020) found no evidence for substantial diurnal variation in the total dayside water vapor column, thus the plausibility of diurnal variations causing such a large spread in column abundances is still considered unlikely.

5.2 Partitioning index

The strongest motivation for the use of a spectral synergy retrieval approach is to access information on the vertical distribution of water vapor. We have shown that during the north polar sublimation period, the magnitude of the near-surface vertical confinement matches model predictions quite well, though discrepancies in the meridional partitioning gradient are significant. For both hemispheres the vertical partitioning remains high and fairly constant (±0.2) for all seasons and latitudes, while displaying a wave-like latitudinal behavior. As water vapor is located at very low altitudes, it is highly affected by complex circulation patterns and waves forced by topographic patterns. This could help forcing the wave-structure of the meridional PI trend. Poleward of the polar cap edge however, the hemispheres differ. In the south the partitioning index is observed to drop for all seasonal intervals except during mid spring. In the north the PI seems to be decreasing at first between 70° and 80°N, and then rapidly increases beyond the polar cap edge, especially so for mid and early spring. This polar cap behavior is well reproduced by the global climate model used to construct the MCD, except during spring for both hemispheres.

The largest relative difference in MCD and synergy vertical confinement in the northern hemisphere is found at mid-latitudes after Ls=150° (see Figure 10). The column abundance, which here never exceeds 20 pr-μm, agrees best with the MCD in this region (though still the synergy finds a lower value), while the obtained synergy partitioning was more than 50% higher than model estimates. This might be indicative of less water escaping through the hygropause than what is estimated in the MCD. For Ls=135°-150°, Figure 12 shows that the MCD and synergy are quite consistent for high latitudes, both finding a PI of 0.7 at 70°N. In the drier low latitudes, where model and synergy agree quite well with regard to column abundances, the partitioning differs significantly. The model suggests the confinement decreases monotonically,

reaching a PI=0.4 at 20°N, while the synergy maintains a strong confinement, obtaining a PI of ~0.7 at 20°N, having barely changed despite a drastic reduction in the total water column. This could suggest that the vertical circulation incorporated in the current model at low latitudes is too strong, causing the MCD partitioning to decrease more quickly towards the equator. The difference could also possibly be due to diurnal "breathing" of the regolith, actively exchanging water with the atmosphere and thus maintaining a near-surface layer. Near-surface meridional transport of sublimated water vapor from the poles could also cause these wave-like trends observed in both hemispheres.

Tamppari and Lemmon (2020) also investigated the near-surface water vapor confinement during early summer in the northern polar region (~70°N) using the a stereo camera on the Phoenix lander. The study indicates that at least 30% of the total column was kept below 2.5 km at all times, and that a well-mixed scenario in this low layer does not fit the data. Vertical profiles and the synergy partitioning index very well supports these findings.

Overall, the synergy finds a more variable vertical partitioning than what the model suggests, which corresponds well with results from solar occultations observations with SPICAM (Maltagliati et al., 2013). This demonstrates that the synergy is particularly useful at mid to low latitudes where atmospheric dynamics influence the vertical partitioning, and over the polar regions where seasonal variations in the vertical partitioning are large and not well reproduced by the model. It would be of great interest to compare the synergistic partitioning with high resolution vertical profiles from for example the solar occultation instruments NOMAD and ACS on TGO. This will be included in future work, although as mentioned earlier, the ability of these instruments to probe the water vapor content in the very low atmosphere is not always present. As the southern hemisphere normally has a higher dust loading than the north, conditions for possibly probing the near-surface atmosphere with TGO are most favorable in the north high latitudes. At low latitudes where we observe large differences between synergy and model, continuously high dust loading will also make direct comparisons between synergy and TGO difficult.

6 Conclusions

Presented here are the results from a spectral synergistic retrieval method applied to water vapor nadir measurements from PFS and SPICAM sampled over seven Martian years. The synergy produces a highly reliable water vapor climatology with geographical and temporal patterns consistent with established literature. When compared to the LMD MCD, the synergy tends to retrieve lower total column abundances, in absolute differences the deviation is biggest for the northern summer sublimation peak, while in relative terms the most significant discrepancies are found at mid latitudes. In the southern hemisphere the synergy and MCD correspond very well. Other differences of note include timing and latitudinal extent of the sublimation onset, which occurs earlier in the MCD, and extends much further equatorward. The synergy finds very comparable column abundances to previous works using single spectral domain approaches with SPICAM and PFS (Fouchet et al., 2007; Trokhimovskiy et al., 2015), somewhat higher values than CRISM (Smith et al., 2009), and slightly lower than TES (Pankine et al., 2010; Smith, 2002).

The ability to extract information on the vertical distribution of water vapor from nadir observations is a unique capability of the spectral synergy approach. The synergy is unable to produce a vertical profile of fine resolution, but it can set reliable constraints on the partitioning

of the water column, differentiating between the near-surface content below 5 km and the rest of the column. Overall, the synergy finds that water is strongly confined to a near-surface layer, and not evenly mixed below the boundary layer. Significant differences between the vertical partitioning over the north and south hemispheres are revealed, where the southern hemisphere exhibits a generally weaker confinement coupled with a stronger seasonal dependence and latitudinal variations than in the north. The near-surface confinement from the synergy overall differs from the MCD especially at low and middle latitudes where the synergy finds a stronger near-surface confinement than MCD estimates. The synergy also finds that the meridional spread of this strong confinement is larger than what the model suggests, maintaining large amounts of near-surface water vapor across most of the northen hemisphere . There appears to be no clear connection between a peak in total column abundance and the amount of vertical partitioning. In general, the synergy finds that the vertical confinement is subject to rapid and local variations, and can change significantly even while the total column abundance remains stable, or remain stable while the column abundance varies.

We have shown that by combining two separate spectral intervals, within which water vapor possesses diagnostic features, increased robustness is brought to the retrieval of column abundances as well as additional information about the vertical content, as compared to the commonly used single-interval retrieval approach. The combination of more accurate column abundances and constraints on the vertical distribution is essential for our understanding of the processes that control the distribution and transport of volatiles in the lower atmosphere.

Considering that current knowledge of the water distribution in the lowermost layer of the atmosphere is mainly based on GCMs, the comparison between the synergy partitioning results and the predictions of the MCD is of particular interest. The significant discrepancies between the two indicate that our understanding of the physics that shape the vertical distribution of atmospheric water on Mars is incomplete.

Acknowledgments

This work was funded by CNES, the Agence Nationale de la Recherche (ANR, PRCI, CE31 AAPG2019, MCUBE project), and background for this project was funded by the European Union's Horizon 2020 Programme under grant agreement UPWARDS-633127. The SPICAM instrument was developed by the Laboratoire Atmospheres, Milieux, Observations Spatiales (LATMOS) in Guyancourt, and the Space Research Institute (IKI) in Moscow. The instrument development was funded by the National Centre for Space Studies of France (CNES), Roscosmos, and RSF (Russian Science Foundation 20-42-0903). The PFS experiment has been built at the “Istituto di Astrofisica e Planetologia Spaziali” (IAPS) of the “Istituto Nazionale di Astrofisica” (INAF) and is currently funded by the Italian Space Agency (ASI) in the context of the Italian participation to the ESA's Mars Express Mission (grant ASI/INAF n. 2018-2-HH.0).

Open Research

The SPICAM and PFS data used in this study can be found at the ESA PSA server https://www.cosmos.esa.int/web/psa/mars-express. The complete processed dataset used to 945 produced the figures in this paper have been published at (Knutsen, 2022) [Dataset]. For model comparisons the Mars Climate Database was used, which can be accessed on this link: http://www-mars.lmd.jussieu.fr/mcd_python/.

References

Aoki, S., Vandaele, A. C., Daerden, F., Villanueva, G. L., Liuzzi, G., Thomas, I. R., Erwin, J. T., Trompet, L., Robert, S., Neary, L., Viscardy, S., Clancy, R. T., Smith, M. D., Lopez-Valverde, M. A., Hill, B., Ristic, B., Patel, M. R., Bellucci, G., Lopez-Moreno, J. -J., & the NOMAD team. (2019). Water Vapor Vertical Profiles on Mars in Dust Storms Observed by TGO/NOMAD. *Journal of Geophysical Research: Planets*, *124*(12), 3482–3497. https://doi.org/10.1029/2019JE006109

Bertaux, J.-L., Korablev, O., Perrier, S., Quémerais, E., Montmessin, F., Leblanc, F., Lebonnois, S., Rannou, P., Lefèvre, F., Forget, F., Fedorova, A., Dimarellis, E., Reberac, A., Fonteyn, D., Chaufray, J. Y., & Guibert, S. (2006). SPICAM on Mars Express: Observing modes and overview of UV spectrometer data and scientific results. *Journal of Geophysical Research*, *111*(E10), E10S90. https://doi.org/10.1029/2006JE002690

Bibring, J.-P., Langevin, Y., Gendrin, A., Gondet, B., Poulet, F., Berthé, M., Soufflot, A., Arvidson, R., Mangold, N., Mustard, J., Drossart, P., & the OMEGA team. (2005). Mars Surface Diversity as Revealed by the OMEGA/Mars Express Observations. *Science*, *307*(5715), 1576–1581. https://doi.org/10.1126/science.1108806

Chicarro, A., Martin, P., & Trautner, R. (2004). *The Mars Express mission: An overview*. *1240*, 3–13.

Christi, M. J., & Stephens, G. L. (2004). Retrieving profiles of atmospheric CO_2 in clear sky and in the presence of thin cloud using spectroscopy from the near and thermal infrared: A preliminary case study: RETRIEVING PROFILES OF CO_2. *Journal of Geophysical Research: Atmospheres*, *109*(D4), n/a-n/a. https://doi.org/10.1029/2003JD004058

Clancy, R. T., Smith, M. D., Lefèvre, F., McConnochie, T. H., Sandor, B. J., Wolff, M. J., Lee, S. W., Murchie, S. L., Toigo, A. D., Nair, H., & Navarro, T. (2017). Vertical profiles of Mars 1.27 μm O 2 dayglow from MRO CRISM limb spectra: Seasonal/global behaviors, comparisons to LMDGCM simulations, and a global definition for Mars water vapor profiles. *Icarus*, *293*, 132–156. https://doi.org/10.1016/j.icarus.2017.04.011

Crismani, M. M. J., Villanueva, G. L., Liuzzi, G., Smith, M. D., Knutsen, E. W., Daerden, F., Neary, L., Mumma, M. J., Aoki, S., Vandaele, A. C., Trompet, L., Thomas, I. R., Ristic, B., Patel, M. R., Bellucci, G., Piccialli,

A., Robert, S., Mahieux, A., Lopez-Moreno, J.-J., … Bauduin, S. (2020). *A Global and Seasonal Perspective of Martian Water Vapor from ExoMars/NOMAD*.

Davies, D. W. (1979). The Vertical Distribution of Mars Water Vapor. *Journal of Geophysical Research*, *84*(B6), 2875–2879.

Davis, B. W. (1969). Some speculations on adsorption and desorption of CO2 in Martian bright areas. *Icarus*, *11*(2), 155–158. https://doi.org/10.1016/0019-1035(69)90040-2

Edwards, D. P., Arellano, A. F., & Deeter, M. N. (2009). A satellite observation system simulation experiment for carbon monoxide in the lowermost troposphere. *Journal of Geophysical Research*, *114*(D14), D14304. https://doi.org/10.1029/2008JD011375

Fanale, F. P., & Cannon, W. A. (1971). Adsorption on the Martian Regolith. *Nature*, *230*(5295), 502–504. https://doi.org/10.1038/230502a0

Farmer, C. B., Davies, D. W., & Laporte, D. D. (1976). Mars: Northern Summer Ice Cap--Water Vapor Observations from Viking 2. *Science*, *194*(4271), 1339–1341. https://doi.org/10.1126/science.194.4271.1339

Fedorova, A., Korablev, O., Bertaux, J.-L., Rodin, A., Kiselev, A., & Perrier, S. (2006). Mars water vapor abundance from SPICAM IR spectrometer: Seasonal and geographic distributions. *Journal of Geophysical Research*, *111*(E9), E09S08. https://doi.org/10.1029/2006JE002695

Fedorova, A., Montmessin, F., Korablev, O., Lefèvre, F., Trokhimovskiy, A., & Bertaux, J. (2021). Multi-Annual Monitoring of the Water Vapor Vertical Distribution on Mars by SPICAM on Mars Express. *Journal of Geophysical Research: Planets*, *126*(1). https://doi.org/10.1029/2020JE006616

Fedorova, A., Montmessin, F., Korablev, O., Luginin, M., Trokhimovskiy, A., Belyaev, D. A., Ignatiev, N. I., Lefèvre, F., Alday, J., Irwin, P. G. J., Olsen, K. S., Bertaux, J.-L., Millour, E., Määttänen, A., Shakun, A., Grigoriev, A. V., Patrakeev, A., Korsa, S., Kokonkov, N., … Wilson, C. F. (2020). Stormy water on Mars: The distribution and saturation of atmospheric water during the dusty season. *Science*, *367*(6475), 297–300. https://doi.org/10.1126/science.aay9522

Fischer, E., Martínez, G. M., Rennó, N. O., Tamppari, L. K., & Zent, A. P. (2019). Relative Humidity on Mars: New Results From the Phoenix TECP Sensor. *Journal of Geophysical Research: Planets*, *124*(11), 2780–2792. https://doi.org/10.1029/2019JE006080

Forget, F., Hourdin, F., Fournier, R., Hourdin, C., Talagrand, O., Collins, M., Lewis, S. R., Read, P. L., & Huot, J.-P. (1999). Improved general circulation models of the Martian atmosphere from the surface to above 80 km. *Journal of Geophysical Research: Planets*, *104*(E10), 24155–24175. https://doi.org/10.1029/1999JE001025

Formisano, V., Angrilli, F., Arnold, G., Atreya, S., Bianchini, G., Biondi, D., Blanco, A., Blecka, M. I., Coradini, A., Colangeli, L., Ekonomov, A., Esposito, F., Fonti, S., Giuranna, M., Grassi, D., Gnedykh, V., Grigoriev, A., Hansen, G., Hirsh, H., … Zasova, L. (2005). The Planetary Fourier Spectrometer (PFS) onboard the European Mars Express mission. *Planetary and Space Science*, *53*(10), 963–974. https://doi.org/10.1016/j.pss.2004.12.006

Fouchet, T., Lellouch, E., Ignatiev, N. I., Forget, F., Titov, D. V., Tschimmel, M., Montmessin, F., Formisano, V., Giuranna, M., Maturilli, A., & Encrenaz, T. (2007). Martian water vapor: Mars Express PFS/LW observations. *Icarus*, *190*(1), 32–49. https://doi.org/10.1016/j.icarus.2007.03.003

Giuranna, M., Formisano, V., Biondi, D., Ekonomov, A., Fonti, S., Grassi, D., Hirsch, H., Khatuntsev, I., Ignatiev, N., Malgoska, M., Mattana, A., Maturilli, A., Mencarelli, E., Nespoli, F., Orfei, R., Orleanski, P., Piccioni, G., Rataj, M., Saggin, B., & Zasova, L. (2005). Calibration of the Planetary Fourier Spectrometer long wavelength channel. *Planetary and Space Science*, *53*(10), 993–1007. https://doi.org/10.1016/j.pss.2005.02.007

Giuranna, M., Viscardy, S., Daerden, F., Neary, L., Etiope, G., Oehler, D., Formisano, V., Aronica, A., Wolkenberg, P., Aoki, S., Cardesín-Moinelo, A., Marín-Yaseli de la Parra, J., Merritt, D., & Amoroso, M. (2019). Independent confirmation of a methane spike on Mars and a source region east of Gale Crater. *Nature Geoscience*, *12*(5), 326–332. https://doi.org/10.1038/s41561-019-0331-9

Haberle, R. M., & Jakosky, B. M. (1990). Sublimation and Transport of Water From the North Residual Polar Cap on Mars. *JOURNAL OF GEOPHYSICAL RESEARCH*, *95*(B2), 1423–1437.

Harri, A. -M., Genzer, M., Kemppinen, O., Gomez-Elvira, J., Haberle, R., Polkko, J., Savijärvi, H., Rennó, N., Rodriguez-Manfredi, J. A., Schmidt, W., Richardson, M., Siili, T., Paton, M., Torre-Juarez, M. D. L., Mäkinen, T., Newman, C., Rafkin, S., Mischna, M., Merikallio, S., … Urqui, R. (2014). Mars Science Laboratory relative humidity observations: Initial results. *Journal of Geophysical Research: Planets*, *119*(9), 2132–2147. https://doi.org/10.1002/2013JE004514

1081 Houben, H., Haberle, R. M., Young, R. E., & Zent, A. P. (1997). Modeling the Martian seasonal water cycle.
1082 *Journal of Geophysical Research: Planets*, *102*(E4), 9069–9083. https://doi.org/10.1029/97JE00046
1083 Jakosky, B. M., & Farmer, C. B. (1982). The seasonal and global behavior of water vapor in the Mars atmosphere:
1084 Complete global results of the Viking Atmospheric Water Detector Experiment. *Journal of Geophysical*
1085 *Research*, *87*(B4), 2999. https://doi.org/10.1029/JB087iB04p02999
1086 Jakosky, B. M., Zent, A. P., & Zurek, R. W. (1997). The Mars Water Cycle: Determining the Role of Exchange with
1087 the Regolith. *Icarus*, *130*(1), 87–95. https://doi.org/10.1006/icar.1997.5799
1088 Kieffer, H., & Titus, T. N. (2001). TES Mapping of Mars' North Seasonal Cap. *Icarus*, *154*(1), 162–180.
1089 https://doi.org/10.1006/icar.2001.6670
1090 Knutsen, E. W. (2022). *Dataset of synergistically retrieved water vapor from SPICAM and PFS nadir observations*
1091 [Data set]. Zenodo. https://doi.org/10.5281/ZENODO.6160793
1092 Korablev, O., Bertaux, J.-L., Fedorova, A., Fonteyn, D., Stepanov, A., Kalinnikov, Y., Kiselev, A., Grigoriev, A.,
1093 Jegoulev, V., Perrier, S., Dimarellis, E., Dubois, J. P., Reberac, A., Van Ransbeeck, E., Gondet, B.,
1094 Montmessin, F., & Rodin, A. (2006). SPICAM IR acousto-optic spectrometer experiment on Mars Express.
1095 *Journal of Geophysical Research*, *111*(E9), E09S03. https://doi.org/10.1029/2006JE002696
1096 Landgraf, J., & Hasekamp, O. P. (2007). Retrieval of tropospheric ozone: The synergistic use of thermal infrared
1097 emission and ultraviolet reflectivity measurements from space. *Journal of Geophysical Research*, *112*(D8),
1098 D08310. https://doi.org/10.1029/2006JD008097
1099 Madeleine, J.-B., Forget, F., Millour, E., Navarro, T., & Spiga, A. (2012). The influence of radiatively active water
1100 ice clouds on the Martian climate: RADIATIVE EFFECT OF MARTIAN CLOUDS. *Geophysical*
1101 *Research Letters*, *39*(23), n/a-n/a. https://doi.org/10.1029/2012GL053564
1102 Maltagliati, L., Montmessin, F., Fedorova, A., Korablev, O., Forget, F., & Bertaux, J.-L. (2011). Evidence of Water
1103 Vapor in Excess of Saturation in the Atmosphere of Mars. *Science*, *333*(6051), 1868–1871.
1104 https://doi.org/10.1126/science.1207957
1105 Maltagliati, L., Montmessin, F., Korablev, O., Fedorova, A., Forget, F., Määttänen, A., Lefèvre, F., & Bertaux, J.-L.
1106 (2013). Annual survey of water vapor vertical distribution and water–aerosol coupling in the martian
1107 atmosphere observed by SPICAM/MEx solar occultations. *Icarus*, *223*(2), 942–962.
1108 https://doi.org/10.1016/j.icarus.2012.12.012

1109 Maltagliati, L., Titov, D. V., Encrenaz, T., Melchiorri, R., Forget, F., Keller, H. L., & Bibring, J.-P. (2011). Annual
1110 survey of water vapor behavior from the OMEGA mapping spectrometer onboard Mars Express. *Icarus*,
1111 *213*(2), 480–495. https://doi.org/10.1016/j.icarus.2011.03.030
1112 Martínez, G. M., Newman, C. N., De Vicente-Retortillo, A., Fischer, E., Renno, N. O., Richardson, M. I., Fairén, A.
1113 G., Genzer, M., Guzewich, S. D., Haberle, R. M., Harri, A.-M., Kemppinen, O., Lemmon, M. T., Smith, M.
1114 D., de la Torre-Juárez, M., & Vasavada, A. R. (2017). The Modern Near-Surface Martian Climate: A
1115 Review of In-situ Meteorological Data from Viking to Curiosity. *Space Science Reviews*, *212*(1–2), 295–
1116 338. https://doi.org/10.1007/s11214-017-0360-x
1117 McElroy, M. B., & Donahue, T. M. (1972). Stability of the Martian Atmosphere. *Science*, *177*(4053), 986–988.
1118 https://doi.org/10.1126/science.177.4053.986
1119 Millour, E., Forget, F., Spiga, A., Vals, M., Zakharov, V., & Montabone, L. (2018). The Mars climate database
1120 (version 5.3). *Paper Pre- Sented at the Mars Science Workshop "From Mars Express to ExoMars", Held*
1121 *27-28 February 2018 at ESAC, Spain, Id.68.*
1122 Montmessin, F., & Ferron, S. (2019). A spectral synergy method to retrieve martian water vapor column-abundance
1123 and vertical distribution applied to Mars Express SPICAM and PFS nadir measurements. *Icarus*, *317*, 549–
1124 569. https://doi.org/10.1016/j.icarus.2018.07.022
1125 Montmessin, F., Forget, F., Rannou, P., Cabane, M., & Haberle, R. M. (2004). Origin and role of water ice clouds in
1126 the Martian water cycle as inferred from a general circulation model. *Journal of Geophysical Research*,
1127 *109*(E10), E10004. https://doi.org/10.1029/2004JE002284
1128 Pan, L., Edwards, D. P., Gille, J. C., Smith, M. W., & Drummond, J. R. (1995). Satellite remote sensing of
1129 tropospheric CO and CH_4: Forward model studies of the MOPITT instrument. *Applied Optics*, *34*(30),
1130 6976. https://doi.org/10.1364/AO.34.006976
1131 Pan, L., Gille, J. C., Edwards, D. P., Bailey, P. L., & Rodgers, C. D. (1998). Retrieval of tropospheric carbon
1132 monoxide for the MOPITT experiment. *Journal of Geophysical Research: Atmospheres*, *103*(D24), 32277–
1133 32290. https://doi.org/10.1029/98JD01828
1134 Pankine, A. A., & Tamppari, L. K. (2015). Constraints on water vapor vertical distribution at the Phoenix landing
1135 site during summer from MGS TES day and night observations. *Icarus*, *252*, 107–120.
1136 https://doi.org/10.1016/j.icarus.2015.01.008

1137 Pankine, A. A., Tamppari, L. K., & Smith, M. D. (2010). MGS TES observations of the water vapor above the
1138 seasonal and perennial ice caps during northern spring and summer. *Icarus*, *210*(1), 58–71.
1139 https://doi.org/10.1016/j.icarus.2010.06.043
1140 Pla-García, J., Rafkin, S. C. R., Martinez, G. M., Vicente-Retortillo, Á., Newman, C. E., Savijärvi, H., de la Torre,
1141 M., Rodriguez-Manfredi, J. A., Gómez, F., Molina, A., Viúdez-Moreiras, D., & Harri, A.-M. (2020).
1142 Meteorological Predictions for Mars 2020 Perseverance Rover Landing Site at Jezero Crater. *Space Science*
1143 *Reviews*, *216*(8), 148. https://doi.org/10.1007/s11214-020-00763-x
1144 Razavi, A., Clerbaux, C., Wespes, C., Clarisse, L., Hurtmans, D., Payan, S., Camy-Peyret, C., & Coheur, P. F.
1145 (2009). Characterization of methane retrievals from the IASI space-borne sounder. *Atmospheric Chemistry*
1146 *and Physics*, *9*(20), 7889–7899. https://doi.org/10.5194/acp-9-7889-2009
1147 Richardson, M. I. (2002). Investigation of the nature and stability of the Martian seasonal water cycle with a general
1148 circulation model. *Journal of Geophysical Research*, *107*(E5), 5031. https://doi.org/10.1029/2001JE001536
1149 Rodgers, C. D. (2000). *Inverse Methods for Atmospheric Sounding: Theory and Practice* (Vol. 2). WORLD
1150 SCIENTIFIC. https://doi.org/10.1142/3171
1151 Rothman, L. S., Gordon, I. E., Babikov, Y., Barbe, A., Chris Benner, D., Bernath, P. F., Birk, M., Bizzocchi, L.,
1152 Boudon, V., Brown, L. R., Campargue, A., Chance, K., Cohen, E. A., Coudert, L. H., Devi, V. M., Drouin,
1153 B. J., Fayt, A., Flaud, J.-M., Gamache, R. R., … Wagner, G. (2013). The HITRAN2012 molecular
1154 spectroscopic database. *Journal of Quantitative Spectroscopy and Radiative Transfer*, *130*, 4–50.
1155 https://doi.org/10.1016/j.jqsrt.2013.07.002
1156 Savijärvi, H., & Harri, A.-M. (2021). Water vapor adsorption on Mars. *Icarus*, *357*, 114270.
1157 https://doi.org/10.1016/j.icarus.2020.114270
1158 Savijärvi, H., McConnochie, T. H., Harri, A.-M., & Paton, M. (2019). Annual and diurnal water vapor cycles at
1159 Curiosity from observations and column modeling. *Icarus*, *319*, 485–490.
1160 https://doi.org/10.1016/j.icarus.2018.10.008
1161 Smith, M. D. (2002). The annual cycle of water vapor on Mars as observed by the Thermal Emission Spectrometer:
1162 MARS WATER VAPOR. *Journal of Geophysical Research: Planets*, *107*(E11), 25-1-25–19.
1163 https://doi.org/10.1029/2001JE001522

Smith, M. D. (2004). Interannual variability in TES atmospheric observations of Mars during 1999–2003. *Icarus*, *167*(1), 148–165. https://doi.org/10.1016/j.icarus.2003.09.010

Smith, M. D., Wolff, M. J., Clancy, R. T., & Murchie, S. L. (2009). Compact Reconnaissance Imaging Spectrometer observations of water vapor and carbon monoxide. *Journal of Geophysical Research*, *114*, E00D03. https://doi.org/10.1029/2008JE003288

Spinrad, H., Münch, G., & Kaplan, L. D. (1963). Letter to the Editor: The Detection of Water Vapor on Mars. *The Astrophysical Journal*, *137*, 1319. https://doi.org/10.1086/147613

Steele, L. J., Lewis, S. R., Patel, M. R., Montmessin, F., Forget, F., & Smith, M. D. (2014). The seasonal cycle of water vapour on Mars from assimilation of Thermal Emission Spectrometer data. *Icarus*, *237*, 97–115. https://doi.org/10.1016/j.icarus.2014.04.017

Tamppari, L. K., Bass, D., Cantor, B., Daubar, I., Dickinson, C., Fisher, D., Fujii, K., Gunnlauggson, H. P., Hudson, T. L., Kass, D., Kleinböhl, A., Komguem, L., Lemmon, M. T., Mellon, M., Moores, J., Pankine, A., Pathak, J., Searls, M., Seelos, F., … Wolff, M. (2010). Phoenix and MRO coordinated atmospheric measurements. *Journal of Geophysical Research*, *115*, E00E17. https://doi.org/10.1029/2009JE003415

Tamppari, L. K., & Lemmon, M. T. (2020). Near-surface atmospheric water vapor enhancement at the Mars Phoenix lander site. *Icarus*, *343*, 113624. https://doi.org/10.1016/j.icarus.2020.113624

Trokhimovskiy, A., Fedorova, A., Korablev, O., Montmessin, F., Bertaux, J.-L., Rodin, A., & Smith, M. D. (2015). Mars' water vapor mapping by the SPICAM IR spectrometer: Five martian years of observations. *Icarus*, *251*, 50–64. https://doi.org/10.1016/j.icarus.2014.10.007

Tschimmel, M., Ignatiev, N. I., Titov, D. V., Lellouch, E., Fouchet, T., Giuranna, M., & Formisano, V. (2008). Investigation of water vapor on Mars with PFS/SW of Mars Express. *Icarus*, *195*(2), 557–575.

Zent, A. P., Hecht, M. H., Cobos, D. R., Wood, S. E., Hudson, T. L., Milkovich, S. M., DeFlores, L. P., & Mellon, M. T. (2010). Initial results from the thermal and electrical conductivity probe (TECP) on Phoenix. *Journal of Geophysical Research*, *115*, E00E14. https://doi.org/10.1029/2009JE003420

Figure 1. The figure caption should begin with an overall descriptive statement of the figure followed by additional text. They should be immediately after each figure. Figure parts are indicated with lower-case letters (a, b, c…). For initial submission, please place

both the figures and captions in the text near where they are cited rather than at the end of the file (not both). At revision, captions can be placed in-text or at the end of the file, and figures should be uploaded separately. Each figure should be one complete, cohesive file (please do not upload sub-figures or figure parts in separate files). Data that supports the figure must be preserved in a repository, included in the Open Research section, and cited in the References. Include detailed information on how to recreate the figure in support of transparency (e.g., Python, R library).

Figure 1. The figure caption should begin with an overall descriptive statement of the figure followed by additional text. They should be immediately after each figure. Figure parts are indicated with lower-case letters (**a, b, c…**). For initial submission, please place both the figures and captions in the text near where they are cited rather than at the end of the file (not both). At revision, captions can be placed in-text or at the end of the file, and figures should be uploaded separately. Each figure should be one complete, cohesive file (please do not upload sub-figures or figure parts in separate files).